

Background reionization history from omniscopes

Sébastien Clesse*

DAMTP, Centre for Mathematical Sciences, Wilberforce Road, Cambridge CB3 0WA, United Kingdom

Laura Lopez-Honorez†

*Max-Planck-Institute for Nuclear Physics, Saupfercheckweg 1, 69117 Heidelberg, Germany and
Theoretische Natuurkunde, Vrije Universiteit Brussel and The
International Solvay Institutes, Pleinlaan 2, B-1050 Brussels, Belgium*

Christophe Ringeval‡

*Centre for Cosmology, Particle Physics and Phenomenology,
Institute of Mathematics and Physics, Louvain University,
2 Chemin du Cyclotron, 1348 Louvain-la-Neuve, Belgium*

Hiroyuki Tashiro§

Physics Department, Arizona State University, Tempe, AZ 85287, USA

Michel H. G. Tytgat¶

*Service de Physique Théorique, CP225 Université Libre de Bruxelles,
Boulevard du Triomphe, 1050 Brussels, Belgium*

(Dated: January 11, 2021)

The measurements of the 21-cm brightness temperature fluctuations from the neutral hydrogen at the Epoch of Reionization (EoR) should inaugurate the next generation of cosmological observables. In this respect, many works have concentrated on the disambiguation of the cosmological signals from the dominant reionization foregrounds. However, even after perfect foregrounds removal, our ignorance on the background reionization history can significantly affect the cosmological parameter estimation. In particular, the interdependence between the hydrogen ionized fraction, the baryon density and the optical depth to the redshift of observation induce nontrivial degeneracies between the cosmological parameters that have not been considered so far. Using a simple, but consistent reionization model, we revisit their expected constraints for a futuristic giant 21-cm omniscopes by using for the first time Markov Chain Monte Carlo (MCMC) methods on multiredshift full sky simulated data. Our results agree well with the usual Fisher matrix analysis on the three-dimensional flat sky power spectrum but only when the above-mentioned degeneracies are kept under control. In the opposite situation, Fisher results can be inaccurate. We show that these conditions can be fulfilled by combining cosmic microwave background measurements with multiple observation redshifts probing the beginning of EoR. This allows a precise reconstruction of the total optical depth, reionization duration and maximal spin temperature. Finally, we discuss the robustness of these results in presence of unresolved ionizing sources. Although most of the standard cosmological parameters remain weakly affected, we find a significant degradation of the background reionization parameter estimation in presence of nuisance ionizing sources.

PACS numbers: 98.80.Cq, 98.70.Vc

I. INTRODUCTION

Among the next generation of cosmological probes, interferometric radio telescopes observing the redshifted 21-cm line associated with the hyperfine transitions of neutral hydrogen atoms have attracted a lot of attention (see Refs. [1–4] for reviews). These telescopes are revolutionary in their design as in the proposed Fast Fourier

Transform Telescope (FFTT) which is conceptually an all digital antennas array imaging the whole visible sky at once [5]. Images would then be reconstructed by a two-dimensional fast Fourier transform over the N antennas signal, i.e. in $N \ln N$ operations. As argued in Ref. [6], compared to the required N^2 pairing in traditional interferometers, the gain could be used to scale up the telescope size and sensitivity thereby allowing measurements of cosmological signals. The first generation of such telescopes is under deployment [7–13]. Although not designed for cosmological purposes, they aim at detecting a cosmological signal from the Epoch of reionization [14–20]. It is still a matter of active research to know if the signal coming from the astrophysical foregrounds can be properly separated from the cosmological one [21–25].

*Electronic address: s.clesse@damtp.cam.ac.uk

†Electronic address: laura.lopez-honorez@mpi-hd.mpg.de

‡Electronic address: christophe.ringeval@uclouvain.be

§Electronic address: hiroyuki.tashiro@asu.edu

¶Electronic address: mtytgat@ulb.ac.be

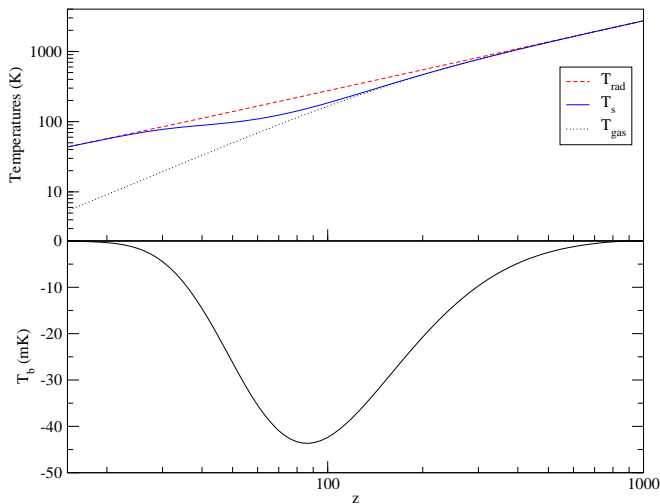


FIG. 1: Background evolution of the neutral hydrogen gas and spin temperatures (top) as a function of the redshift during the dark ages. The spin temperature T_s being defined as $n_1/n_0 = 3 \exp[-\hbar\omega_{21}/(k_B T_s)]$ where n_0 and n_1 denote the number density of atoms in the singlet and triplet hyperfine states, respectively. The bottom panel shows the resulting brightness temperature.

One should indeed keep in mind that the former is actually a few order of magnitude stronger than the latter and this has triggered interest in the cross-correlation of the 21-cm signal with much cleaner data such as the Cosmic Microwave Background (CMB) or galaxy surveys [26–30].

The physical origin of the cosmological 21-cm radiation lies in the differential cooling induced by the expansion of the Universe on relativistic and non-relativistic gases. After recombination, one would naively expect the temperature of neutral hydrogen T_{gas} to decrease in $1/a^2$, where a is the Friedmann-Lemaître-Robertson-Walker (FLRW) scale factor, which is faster than the radiation temperature T_{rad} scaling as $1/a$. As a result, the neutral hydrogen gas becomes cool enough to be able to absorb CMB photons by a spin flip hyperfine transition at a wavelength of 21-cm. Tuning a radio telescope at the corresponding redshifted frequency allows, in principle, to probe the density fluctuations of neutral hydrogen over the sky and at any redshift, hence the so-called cosmological tomography [31, 32]. In reality, the situation is a bit more complex and one has to take into account the evolution of the Boltzmann distribution of neutral hydrogen due to the collisions with the residual electrons, protons and absorption versus stimulated emission of CMB photons [33–36]. The background evolution can nevertheless be numerically derived and we have plotted in Fig. 1 the resulting brightness temperature evolution.

For an assumed generic set of cosmological parameters, taken from the Wilkinson Microwave Anisotropy Probe (WMAP) seven-year data [37], the absorption is maximal around a redshift of $z \simeq 10^2$. Notice that at lower redshifts, the spin temperature is driven again towards

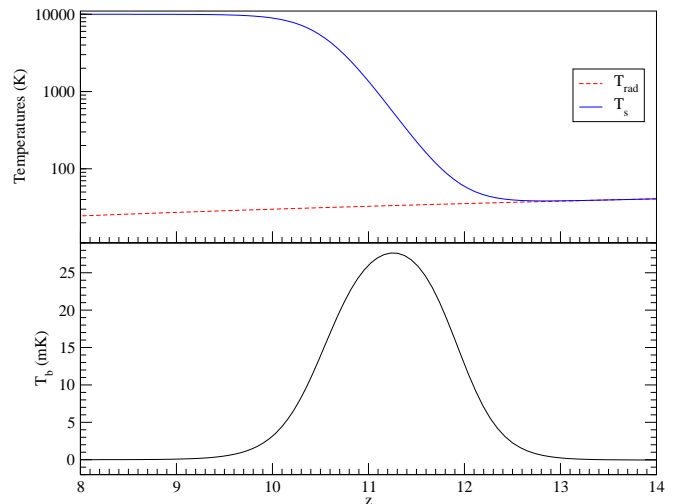


FIG. 2: Reionization driven spin temperature (top) and brightness temperature (bottom) with respect to the observation redshift. The reionization model is described in Sec. II B ($\tau = 0.088$).

the photon temperature and the signal vanishes till the EoR. The evolution of neutral hydrogen density fluctuations can similarly be predicted during the dark ages by using the theory of cosmological perturbations [38–40]. Provided the length scales of interest remain in the linear regime, the theoretical predictions for the 21-cm power spectra are neat [41–44]. Being three-dimensional in nature, the information content is huge and have been used to forecast constraints on various cosmological models such as non-Gaussianities [45–48], cosmic strings [49–52], dark matter signatures [53–57], modified gravity [58] and inflation [59–62].

As already mentioned, in addition to having a small amplitude compared to foregrounds, the dark ages signal is redshifted to wavelengths of typically twenty meters and it is not obvious that it may actually be used for cosmology in a foreseeable future. One very futuristic approach would be to build those radio telescopes on the Moon [63]. A more reasonable approach is the possibility to probe the hydrogen density fluctuations with the 21-cm line at the EoR [64–66]. This time, the exciting photons are coming from reionization sources (stars or quasars) instead of the CMB and are expected to produce an efficient spin states population inversion. This results into $T_s \gg T_{\text{rad}}$ and generates an emission line at a much smaller redshifted wavelength. We have plotted the expected evolution of the brightness temperature during the EoR in Fig. 2 for a simple reionization model that we describe in Sec. II B.

The resulting signal is around 25 mK in amplitude, which is of the same order than those coming from the dark ages, but at a higher frequency thereby rendering its detection more likely. However, the theoretical predictions are now far less neat due to the additional as-

trophysical uncertainties associated with the way reionization proceeds [67, 68]. However since 21 cm data are three-dimensional by nature, it has been shown in Refs. [69, 70] that the redshift evolution could be used to efficiently eliminate the expected foregrounds while still keeping some of the so-called longitudinal modes for cosmology.

Forecasting the 21-cm constraints for cosmology is usually made from Fisher matrix analysis which merely assumes the likelihood to be Gaussian around the best fit. Provided the parameters are well constrained, the method is fast and accurate [71]. However, as noted in Ref. [44], some model parameters linked to reionization, such as the optical depth or the hydrogen ionized fraction, can be completely degenerated from the 21-cm point of view and factorize out of the Fisher matrix. In a realistic situation, this should not be the case as all reionization parameters are uniquely determined by the background reionization history. One may therefore wonder how their correlations to the standard cosmological parameters affect the forecasts.

In Refs. [20, 72], the problem of reconstructing the background reionization history is specifically addressed in the context of future 21-cm experiments that would be devoted to the global signal, i.e. the homogeneous mode. Here, we would like to discuss this issue for the 21-cm FFTT-like experiments which are poorly, if not at all, sensitive to the constant mode. In that situation, the cosmological brightness fluctuations $\delta T_b(\mathbf{x}, z)$ have simultaneously a dependence in both the background evolution and spectral shape. This question is peculiar to 21-cm observables because the homogeneous mode $T_b(z)$ depends on various cosmological parameters, and when concerned with EoR, on the reionization (see Sec.II A). Let us notice that such a situation does not occur for CMB not only because T_{cmb} is measured, but because it is uniquely determined by Ω_γ .

In this context, we would like to quantify how cosmological forecasts are affected by the background reionization history, and if it is possible for omniscopes to constrain the reionization parameters. For this purpose, we consider a giant FFTT-like ground-based instrument and assume that most of the foregrounds can indeed be eliminated using redshift evolution. As a result, we will be keeping only a few redshift slices for our forecasts, eventually marginalizing over some nuisance ionization spectra modelled as in Ref. [44]. We consider a simple reionization model for which the time evolution of the spin temperature, hydrogen ionized fraction and optical depth are given as a function of some extra parameters. In this manner, it is imposed that they are intrinsically correlated by reionization physics. As already mentioned, in order to go beyond Fisher matrix, we use MCMC methods over a modified version of the CAMB 21-cm code [42, 43, 73] which includes the Epoch of Reionization as well as some nuisance ionization spectra. This allows us to use and compare both Fisher matrix analysis and full sky simulated data coupled to MCMC

methods [74].

The paper is organized as follows. In Sec. II, we present the reionization and telescope models used in the analysis while the methodology and results are presented in Sec. III. Starting from one redshift slice only, we show that the reionization induced degeneracies damage, and sometime prevent, the determination of some cosmological parameters, such as the baryon density. In these situations, we also find that a Fisher analysis can be inaccurate for some strongly correlated parameters. Combining a few redshifts, which sample the beginning of reionization, improves the situation but does not compete with a Planck-like CMB experiment. However, we show in Sec. III C 3, that combining 21-cm and CMB lifts almost all those degeneracies thereby improving the overall accuracy by an order of magnitude. In that situation our MCMC results match with the usual Fisher matrix analysis while the underlying reionization model can be completely determined. Finally, we show that these results may be mitigated by the presence of toy nuisance reionization spectra.

II. REIONIZATION AND TELESCOPE MODELS

A. 21-cm signal from the EoR

1. Background

Assuming a small emission line profile, the 21-cm brightness temperature during the EoR and at a given observed energy ϵ is given by [42]

$$T_b(\epsilon) = (1 - e^{-\tau_\epsilon}) \left. \frac{T_s - T_{\text{rad}}}{1 + z} \right|_{\eta_\epsilon}, \quad (1)$$

where τ_ϵ is the optical depth to 21-cm

$$\tau_\epsilon = \left. \frac{3\hbar c^3 A_{10} n_{\text{HI}}(\eta)}{16k_B \nu_{21}^2 T_s(\eta) H(\eta)} \right|_{\eta_\epsilon}. \quad (2)$$

All quantities are evaluated at the conformal time $\eta = \eta_\epsilon$ at which $\epsilon = a(\eta_\epsilon) E_{21} = 2\pi a(\eta_\epsilon) \hbar \nu_{21}$, ν_{21} being the rest frame frequency of the 21-cm spin flip atomic transition and a is the scale factor. In the following, we use natural units $k_B = \hbar = c = 1$. In Eq. (2), $A_{10} \simeq 2.869 \times 10^{-15} \text{ s}^{-1}$ is the Einstein coefficient of spontaneous emission, $n_{\text{HI}}(\eta)$ the density of neutral hydrogen atoms and $H(\eta)$ the Hubble parameter. Introducing the neutral fraction $x_{\text{H}} \equiv n_{\text{HI}}/(n_{\text{HI}} + n_{\text{i}})$, with n_{i} the number density of ionized hydrogen, one can express the density of neutral hydrogen in terms of the cosmological parameters today as

$$n_{\text{HI}}(z) = x_{\text{H}}(z) \frac{3\Omega_b H_0^2 (1 - Y)}{8\pi G_N m_{\text{H}}} (1 + z)^3, \quad (3)$$

where $Y \simeq 0.24$ is the helium mass fraction¹ and m_{H} the mass of the hydrogen atom. During reionization, one assumes that T_{s} is driven to high values due to ionizing sources [68] such that one can expand Eq. (1) in

$$T_{\text{b}} = aT_{\epsilon} - a\frac{T_{\epsilon}}{T_{\text{s}}}\left(T_{\text{rad}} + \frac{1}{2}T_{\epsilon}\right) + \mathcal{O}\left(\frac{T_{\epsilon}}{T_{\text{s}}}\right)^2, \quad (4)$$

where

$$T_{\epsilon} \equiv \tau_{\epsilon}T_{\text{s}} = \frac{9A_{10}M_{\text{Pl}}^2\Omega_{\text{b}}H_0^2(1-Y)}{16\nu_{21}^2m_{\text{H}}a^3(\eta_{\epsilon})H(\eta_{\epsilon})}x_{\text{H}}(\eta_{\epsilon}). \quad (5)$$

In the limit $T_{\text{s}} \gg T_{\epsilon}$, $T_{\text{b}} \simeq aT_{\epsilon}$. The brightness temperature is thus positive (emission line), does not depend anymore on the spin temperature and is directly proportional to x_{H} . Up to the metric fluctuations, this is also the case for the linear perturbations δT_{b} which directly probe the neutral hydrogen fluctuations. However, the approximation $T_{\text{s}} \gg T_{\epsilon}$ cannot hold at the beginning of reionization as T_{s} should continuously rise from the dark ages value to its maximum value deep in the reionization era. As a result, it is far from evident that there exists a redshift range for which this approximation is fully consistent. Actually, even for a spin temperature $T_{\text{s}} \sim 10^3$ K, one can check that differences at the percent level already arise between Eq. (1) and the leading term of Eq. (4). For these reasons, in this paper, we keep the complete dependence in T_{s} and T_{rad} and assume a simple, but consistent, model of reionization to parametrize the spin temperature evolution (see Fig. 2 and Sec. II B).

2. Linear perturbations

The brightness temperature fluctuations can be obtained by solving the Boltzmann equations driving the evolution of the 21-cm photons in a perturbed FLRW space-time. This has already been done by Lewis and Challinor during the dark ages in Ref. [42]. We have followed their approach while adding the contributions of the hydrogen ionized fraction perturbations coming from the reionization sources. For this purpose, we have modified the publicly available CAMB code [73, 75] and numerically solved the full Boltzmann equations incorporating all the linear order effects discussed in Ref. [42], i.e. neglecting only anisotropies higher than dipole photon ones and any broadening of the emission line profile. The multipoles components of the 21-cm distribution function actually used in the next sections have been written down in Appendix A.

In order to illustrate the physical processes at work, it is nevertheless convenient to approximate the perturbed Boltzmann distribution in the small scale limit and at

leading order in τ_{ϵ} . Let us emphasize again that these approximations are not made in the actual forecasts of Sec. III. Along the line-of-sight direction $\hat{\mathbf{n}}$, at the measured energy ϵ , one gets

$$\delta T_{\text{b}}(\mathbf{x}, \hat{\mathbf{n}}, \epsilon) \simeq T_{\text{b}}e^{-\tau_{\epsilon}}\left[\Delta_{\text{s}} - \frac{1}{aH}\hat{\mathbf{n}} \cdot \frac{\partial \mathbf{v}}{\partial \eta}\right]_{\eta_{\epsilon}}, \quad (6)$$

where the Δ_{s} is monopole source

$$\Delta_{\text{s}} \equiv \Delta_{\text{HI}} + \frac{T_{\text{rad}}}{T_{\text{s}} - T_{\text{rad}}}(\Delta_{T_{\text{s}}} - \Delta_{T_{\text{rad}}}), \quad (7)$$

and all $\Delta_x \equiv \delta x/x$ stand for relative perturbations. The second term of Eq. (6) encodes the redshift distortions due to the perturbations \mathbf{v} in the (baryonic) gas relative velocity to the observer. As shown in Ref. [42], Thompson scattering suppresses the 21-cm brightness on all scales and is responsible of the exponential term in Eq. (6), $\tau_{\epsilon}(\eta_{\epsilon})$ being the Thompson optical depth to the redshift of observation (not to be confused with τ_{ϵ}). During the dark ages, $x_{\text{H}} \simeq 1$ and the perturbations Δ_{HI} in the neutral hydrogen directly trace the baryonic perturbations $\Delta_{\text{b}} \equiv \delta n_{\text{b}}/n_{\text{b}}$. At the EoR, the ionizing sources on their own are expected to induce new perturbations in the neutral fraction such that $\Delta_{\text{HI}} = \Delta_{x_{\text{H}}} + \Delta_{\text{b}}$ (at fixed helium fraction), or, in terms of the *hydrogen* ionized fraction x_{i} (not to be confused with the total ionized fraction x_{e})

$$\Delta_{\text{HI}} = \Delta_{\text{b}} - \frac{x_{\text{i}}}{x_{\text{H}}}\Delta_{x_{\text{i}}}, \quad (8)$$

where $\Delta_{x_{\text{i}}}$ is the relative ionized fraction perturbation. Notice that the ionizing sources are also generating additional spin temperature perturbations through their effects on the gas temperature and Lyman- α emission [16, 67, 76]. However, they are not considered here for simplicity. The expression for the brightness fluctuations can be further simplified by assuming that the regime $T_{\text{s}} \gg T_{\text{rad}}$ holds at the redshift of interest. In this limit, Eq. (6) reads in Fourier space

$$\delta T_{\text{b}}(\mathbf{k}, \hat{\mathbf{n}}, \epsilon) \simeq e^{-\tau_{\epsilon}}\tilde{T}_{\text{b}}(\epsilon)\left[x_{\text{H}}\Delta_{\text{b}} - x_{\text{i}}\Delta_{x_{\text{i}}} - \mu^2x_{\text{H}}\Delta_{\text{v}}\right]_{\eta_{\epsilon}}, \quad (9)$$

where $\mu \equiv \mathbf{k} \cdot \hat{\mathbf{n}}/k$ and $\tilde{T}_{\text{b}} \equiv T_{\text{b}}/x_{\text{H}}$ is the background brightness temperature if hydrogen were fully neutral, i.e. from Eq. (4) and (5)

$$\tilde{T}_{\text{b}}(\epsilon) = \frac{9A_{10}M_{\text{Pl}}^2\Omega_{\text{b}}H_0^2(1-Y)}{16\nu_{21}^2m_{\text{H}}a^2(\eta_{\epsilon})H(\eta_{\epsilon})}. \quad (10)$$

In Eq. (9), we have introduced the perturbed quantity

$$\Delta_{\text{v}} \equiv \frac{kv}{aH}, \quad (11)$$

where v is the Fourier transform of the radial baryon velocity. Assuming that at EoR we can neglect the time evolution of the gravitational potentials [39], one can further approximate $\Delta_{\text{v}} \simeq -\Delta_{\text{b}}$.

¹ Notice that the helium fraction affects significantly the brightness temperature for a given Ω_{b} .

3. Three-dimensional power spectrum

The three-dimensional power spectrum of the brightness temperature fluctuations, $P_{\delta T_b}$, is defined via

$$\langle \delta T_b(\mathbf{k}) \delta T_b(\mathbf{k}') \rangle = (2\pi)^3 \delta^3(\mathbf{k} - \mathbf{k}') P_{\delta T_b}(\mathbf{k}), \quad (12)$$

where the brackets denote the ensemble average. One can also define

$$\mathcal{P}(\mathbf{k}) \equiv \frac{k^3}{2\pi^2} P(\mathbf{k}), \quad (13)$$

such that the isotropic real space variance simplifies to

$$\langle \delta T_b^2(x) \rangle = \int d \ln k \mathcal{P}(k). \quad (14)$$

Using Eq. (9), the power spectrum reduces to [44]

$$P_{\delta T_b}(\mathbf{k}) = e^{-2\tau_c} \tilde{T}_b^2 \left\{ x_H^2 P_b(k) + x_i^2 P_{ii}(k) - 2x_H x_i P_{ib}(k) \right. \\ \left. + 2\mu^2 [x_H x_i P_{vi}(k) - x_H^2 P_{vb}(k)] + \mu^4 x_H^2 P_v(k) \right\}, \quad (15)$$

where the (cross) power spectra are defined as in Eq. (12) between the perturbation variables Δ_b , Δ_v and Δ_{x_i} . The key point of Eq. (15) is that the μ^4 component depends on the baryonic matter power spectrum only since $P_v \simeq P_b$, which is completely fixed by cosmology. On the contrary, the power spectra $P_{ii}(k)$, $P_{vi}(k)$ and $P_{ib}(k)$ are reionization dependent and considered as nuisances. As seen in Eq. (15), they appear only with an angular dependence in μ^0 or μ^2 , but not in μ^4 . This property is expected to play a crucial role in the separation of the cosmological signal from those astrophysical contaminants [77, 78]. Following these references, we can therefore define

$$P_0(k) \equiv x_H^2 P_b(k) + x_i^2 P_{ii} - 2x_H x_i P_{ib}(k), \\ P_2(k) \equiv 2 [x_H x_i P_{vi}(k) - x_H^2 P_{vb}(k)], \quad (16) \\ P_4(k) \equiv x_H^2 P_v(k),$$

such that Eq. (15) simplifies

$$P_{\delta T_b}(\mathbf{k}) = e^{-2\tau_c} \tilde{T}_b^2 [P_0(k) + \mu^2 P_2(k) + \mu^4 P_4(k)]. \quad (17)$$

Let us emphasize that the power spectrum $P_{\delta T_b}(\mathbf{k})$ is not directly accessible to 21-cm experiments, i.e. one cannot directly measure the comoving position \mathbf{r} of the signal, Fourier dual of the wave vector \mathbf{k} . Any experiment can however determine angular separations Θ in the sky, and signal frequency differences F around any 21-cm line of redshift z . In this paper, we consider a FFTT which is designed to map a hemisphere. Following Ref. [44], one can divide the sky into small patches for which the flat sky approximation is valid. In this limit, Θ and F in each patch are directly proportional to the variations of the comoving distance's components perpendicular \mathbf{r}_\perp and parallel r_\parallel to the line-of-sight with respect to the central redshift z ,

$$\Theta = \frac{\mathbf{r}_\perp}{D_A(z)}, \quad F = \frac{r_\parallel}{y(z)}. \quad (18)$$

Here D_A stands for the angular comoving distance, given in a flat Universe by

$$D_A(z) = \int_0^z \frac{1}{H(z')} dz', \quad (19)$$

and $y(z)$ is the conversion factor between comoving distances and frequency intervals,

$$y(z) = \frac{\lambda_{21}(1+z)^2}{H(z)}. \quad (20)$$

In Eq. (6), the 21-cm brightness temperature fluctuations have been obtained in terms of \mathbf{k} while it would be more convenient to describe it in terms of Fourier duals of the frequency differences and of the angular separations denoted as u_\parallel and \mathbf{u}_\perp , respectively. Their relation to the comoving wave vector \mathbf{k} reads

$$\mathbf{u}_\perp = D_A(z) \mathbf{k}_\perp, \quad u_\parallel = y(z) k_\parallel. \quad (21)$$

As a consequence, the observable three-dimensional power spectrum of the 21-cm brightness temperature is measured in \mathbf{u} space and reads

$$P_{\delta T_b}(\mathbf{u}) = \frac{P_{\delta T_b}[\mathbf{k}(\mathbf{u})]}{D_A^2(z) y(z)}. \quad (22)$$

4. Angular power spectrum

Out of the flat sky approximation, one has to derive the angular power spectrum of the 21-cm brightness temperature for each observed redshift z . From an infinitely thin shell at redshift z , corresponding to the observed 21-cm energy $\epsilon(z)$, the angular power spectrum is given by [42]

$$C_\ell(z) = \frac{2}{\pi} \int F_\ell(\epsilon, k) F_\ell(\epsilon, k) k^2 dk, \quad (23)$$

where $F_\ell(\epsilon, k)$ are the multipole components today of the 21-cm photon distribution function. Their expressions have been derived in Ref. [42] by solving the Boltzmann equation during the dark ages for the perturbed photon distribution function (see Appendix A). At EoR, these equations remain unchanged but the fractional fluctuations Δ_{HI} appearing in Eq. (A2) are now given by Eq. (8). The monopole source is still defined as in Eq. (7) with a background spin temperature that can, however, be driven by the new ionizing sources.

One can recover the usual approximated results by keeping only the monopole and redshift distortion terms. In that case, the angular power spectrum simplifies to

$$C_\ell(z) \simeq 4\pi e^{-2\tau_c(z)} \tilde{T}_b^2 \int d \ln k \left\{ \mathcal{P}_0(k) [j_\ell(\Delta\eta_\epsilon)]^2 \right. \\ \left. - \mathcal{P}_2(k) j_\ell(k\Delta\eta_\epsilon) j_\ell''(k\Delta\eta_\epsilon) + \mathcal{P}_4(k) [j_\ell''(k\Delta\eta_\epsilon)]^2 \right\}, \quad (24)$$

which is the equivalent of Eq. (17) on the full sky. In the following, the full sky results are derived by using a modified version of the **CAMB** code [42, 73, 74] in which we have implemented the above-mentioned extra sources associated with the EoR. This allows to integrate the complete equations of motion (see Appendix A) under a given model of reionization which is discussed in the next section. In addition, we consider the same finite width Gaussian window functions in frequency as in Ref. [42], such that the observed angular power spectrum is actually given by their convolution with Eq. (23). Finally, we have cross-checked our computations by comparing the modified **CAMB** results with an independent code directly integrating Eq. (24). As expected, both spectra match at small angular scales and for narrow window function (see Fig. 3).

B. Reionization model

1. Background

In order to model the EoR, we consider a toy model similar to the one used for CMB data analysis [37], namely a smooth transition from the dark ages ionized fraction to complete reionization. A similar model has also been considered for 21-cm analysis of the global reionization signal in Ref. [20, 72]. CMB polarization measurements allow to infer the value of τ , the Compton optical depth to reionization defined as

$$\tau = \int_0^{\eta_0} a(\eta) n_e(\eta) \sigma_T d\eta. \quad (25)$$

In this expression, σ_T is the Thomson scattering cross section while n_e stands for the number density of free electrons. As explicit in Eqs. (17) and (24), Thomson scattering at EoR affects the overall amplitude of the 21-cm power spectra through $\tau_c(z)$, the optical depth to the redshift of observation. Let us stress that the latter is defined as in Eq. (25) but starting at the conformal time η_e . Equations (17) and (24) make clear that, already at the background level, the 21-cm signal at EoR is strongly correlated with the total optical depth τ that can be measured in CMB experiments. In order to make the dependency explicit, we have used and extended the reionization model used in **CAMB** [73]. In this model, and denoting by $x_e \equiv n_e/(n_{\text{H}} + n_{\text{i}})$ the total ionized fraction²,

reionization occurs according to

$$x_e = \frac{1 + f_{\text{He}}}{2} \left\{ 1 + \tanh \left[\frac{(1 + z_{\text{reio}})^{3/2} - (1 + z)^{3/2}}{\Delta_{\text{reio}}} \right] \right\} + \frac{f_{\text{He}}}{2} \left[1 + \tanh \left(\frac{z_* - z}{\Delta_*} \right) \right] + x_e|_{\text{rec}}, \quad (26)$$

where $f_{\text{He}} \simeq 0.08$ is the helium density fraction, assumed to become firstly ionized at the same time as hydrogen³ and doubly ionized at $z = z_*$. The parameter Δ_{reio} fixes the duration of reionization while z_{reio} refers to its central redshift. The second term encodes the complete helium ionization and remains always very small. It has been kept only for consistency with previous CMB analysis with the same fixed values of $z_* = 3.5$ and $\Delta_* = 0.5$. The last term is a constant encoding the residual ionized fraction from recombination which does not exceed a few thousandths. From Eq. (26), one immediately gets the associated optical depth by using Eq. (25) and conversely. The choice of the power 3/2 in Eq. (26) is made such that for all Δ_{reio} , the corresponding value of τ remains equal to the one that would be associated with an instantaneous reionization at $z = z_{\text{reio}}$ (see Ref. [73]). It can be convenient to express Δ_{reio} in terms of redshift duration and we will use in the following the parameter Δ_z defined by

$$\Delta_z \equiv \frac{2}{3} \frac{\Delta_{\text{reio}}}{\sqrt{1 + z_{\text{reio}}}}. \quad (27)$$

For our purpose, Eq. (26) already fixes the evolution of the hydrogen neutral and ionized fraction, respectively, as

$$\begin{aligned} x_{\text{H}} &= 1 - x_{\text{i}}, \\ x_{\text{i}} &= x_{\text{i}}|_{\text{rec}} + \frac{1 - x_{\text{i}}|_{\text{rec}}}{2} \left\{ 1 + \tanh \left[\frac{(1 + z_{\text{reio}})^{3/2} - (1 + z)^{3/2}}{\Delta_{\text{reio}}} \right] \right\}. \end{aligned} \quad (28)$$

Concerning the spin temperature, since it is expected to be physically driven by ionizing sources, we have chosen for simplicity a similar evolution:

$$\begin{aligned} T_{\text{s}}(z) &= T_{\text{s}}^{\text{da}} + \frac{T_{\text{s}}^{\text{max}} - T_{\text{s}}^{\text{da}}}{2} \\ &\times \left\{ 1 + \tanh \left[\frac{(1 + z_{\text{reio}})^{3/2} - (1 + z)^{3/2}}{\Delta_{\text{reio}}} \right] \right\}. \end{aligned} \quad (29)$$

The quantity T_{s}^{da} is the spin temperature value during the dark ages, just before reionization starts, and it is completely fixed by the cosmological model. Let us emphasize that in a more realistic situation the redshift functional dependence of T_{s} is not the same as the

² It can therefore be greater than one when helium becomes ionized.

³ $f_{\text{He}} = \frac{m_{\text{H}}}{m_{\text{He}}} \frac{Y}{1 - Y}$.

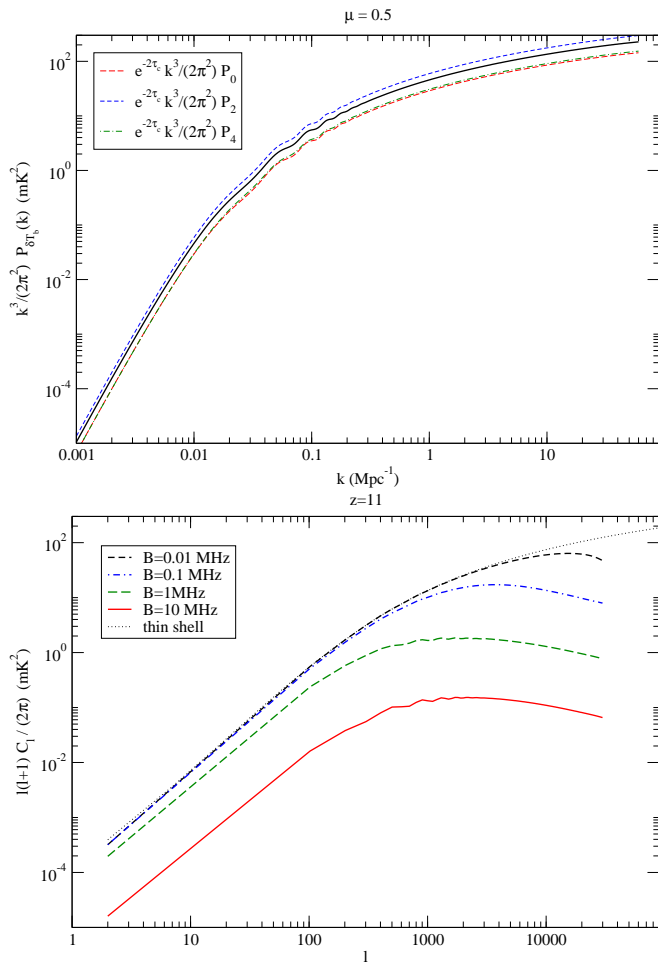


FIG. 3: Three-dimensional power spectra $\mathcal{P}_{\delta T_b}(k)$ (top) and angular power spectrum C_ℓ (bottom) for an observation redshift $z = 11$ and assuming no foregrounds. The cosmological parameters are the ones of Sec. II B ($\tau = 0.088$, $z_{\text{reio}} \simeq 10.54$, $x_{\text{H}} \simeq 0.87$, $T_s \simeq 1360$ K). The C_ℓ are convolved with Gaussian window functions whose standard deviation is given by the bandwidth B . Large bandwidths damp the overall power but render the acoustic oscillations visible [42]. The thin shell limit has been obtained by integrating Eq. (24).

ionized fraction, especially during the first stages of the reionization processes [2, 4]. For our purpose, Eq. (29) introduces only one extra parameter, T_s^{max} , which gives the maximum spin temperature value once the Universe is completely reionized. Unless specified, we assume in the following the fiducial $T_s^{\text{max}} = 10000$ K.

Figure 3 shows the theoretical three-dimensional and angular power spectra computed at $z = 11$ for the background cosmological and reionization models just described. The top curve in the bottom panel has been obtained by a direct integration of Eq. (24), i.e. including only monopole and redshift distortions. As expected, it matches in shape and amplitude with three-dimensional power spectrum (top panel). The other angular spectra have been computed with our modified version of the

z	x_{H}	N_{ii}	R_{ii} (Mpc)	α_{ii}	γ_{ii}	N_{ib}	R_{ib} (Mpc)	α_{ib}
11	0.87	16.0	1.3	-1.4	0.5	3.96	0.57	-0.27

TABLE I: Parameter values for the nuisance ionization power spectra at $z = 11$, linearly interpolated from Ref. [44].

CAMB code and are convolved in frequency with Gaussian window function of bandwidth B . As discussed in Ref. [42], larger values of the bandwidth damps the overall power but allows the sampling of acoustic oscillations. In the limit $B \rightarrow 0$, one recovers Eq. (24).

2. Ionizing sources

At the perturbative level, the shape and time evolution of P_{ib} , P_{vb} and P_{ii} are expected to depend on the reionization details. Following Ref. [44], we consider here only the spectra associated with the fluctuations in the ionized fraction and adopt a phenomenological parametrization of these power spectra as

$$\begin{aligned} P_{\text{ii}}(k) &= N_{\text{ii}} \left[1 + \alpha_{\text{ii}} k R_{\text{ii}} + (k R_{\text{ii}})^2 \right]^{-\gamma_{\text{ii}}/2} P_{\text{b}}(k), \\ P_{\text{ib}}(k) &= N_{\text{ib}} \exp \left[-\alpha_{\text{ib}} k R_{\text{ib}} - (k R_{\text{ib}})^2 \right] P_{\text{b}}(k) \end{aligned} \quad (30)$$

where N_{ii} , N_{ib} are normalization constants and α_{ii} , α_{ib} , γ_{ii} , R_{ii} and R_{ib} are model parameters to be adjusted to match numerical simulations [79, 80]. Since these spectra are nuisance, we moreover approximate $P_{\text{vi}}(k) \simeq -P_{\text{ib}}(k)$ from Eq. (11). Taking the fiducial cosmological parameter values $\Omega_{\text{b}} h^2 = 0.023$, $\Omega_{\text{dm}} h^2 = 0.115$, $h = 0.71$ and $\tau = 0.088$, the reionization model of the previous section gives $z_{\text{reio}} = 10.536$ at which the hydrogen neutral fraction $x_{\text{H}}(z_{\text{reio}}) = 0.5$.

In Table I, we give the parameter values associated with the reionization power spectra of Refs. [44, 79] at $z = 11$. These values will be used in the following to test the robustness of the parameter estimation with respect to the presence of extra ionizing sources. Although not rigorously correct, we assume that the redshift dependence of the ionizing power spectra is completely given by the ionized fractions $x_{\text{H}}(z)$ and $x_{\text{i}}(z)$, i.e. that the parameters of Table I remain constant during the beginning of the EoR. Notice that the ionized fraction dependency is not included in N_{ii} and N_{ib} such that the time evolution of the ionizing power spectra is well behaved, i.e. vanishes as soon as $x_{\text{i}} \rightarrow 0$.

In Fig. 4, we have plotted these spectra for $z = 11$, as well as their effects on the expected three-dimensional and angular power spectrum. For this redshift, $x_{\text{H}} x_{\text{i}} P_{\text{ib}}$ dominates and reduces the overall power whereas at low redshift we would find extra power coming for the domination of $x_{\text{i}}^2 P_{\text{ii}}$. Finally, let us emphasize that we have not included, for simplicity, the contributions coming from the spin and gas temperature fluctuations that would be associated with the ionizing sources. However, such an improvement could be made in a similar way.

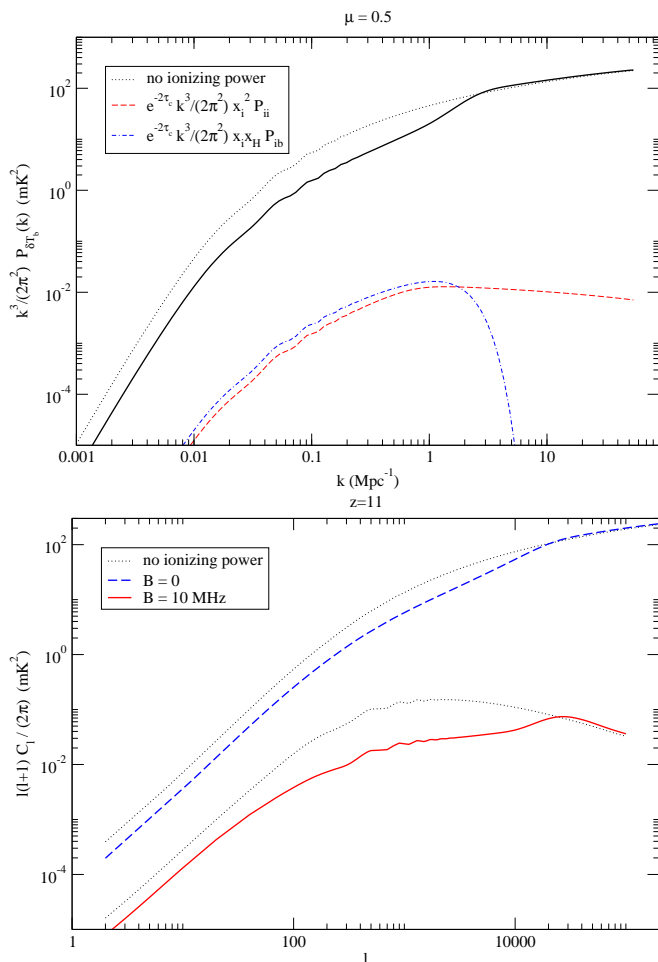


FIG. 4: Effects of the reionization power spectra at $z = 11$ (see Table I) on the three-dimensional power spectrum $\mathcal{P}_{\delta T_b}$ (top). The bottom panel shows the reionization induced deviations on the angular power spectrum C_ℓ , both for the thin shell approximation and a window function of bandwidth $B = 10$ MHz.

C. Fast Fourier Transform Telescope

In this section we give the ideal characteristics chosen for the omniscopes used in the following forecasts. The FFTT we are considering is in between the original design introduced in Ref. [5] and a very futuristic concept used in Ref. [60] for probing the dark ages. Detecting signals from the EoR does not require gigantic array as the redshifted 21-cm wavelength from z_{reio} is about two meters. However, pushing up the scale of the original FFTT concept from 1 km to 10 km would allow to probe the end of the dark ages, i.e. up to redshift 20–30. In such a design, the sensitivity to dark age signals is quite low and forecasts suggest that this would not be competitive with CMB (see Sec. III B). However, including those redshifts into a multi-redshift analysis allows to slice in details the transition to the EoR, and as discussed

in Sec. III C, allows a good inference of the background reionization properties such as duration or spin temperature evolution.

1. Beam, noise and ionosphere

We consider a squared FFTT design of $D = 10$ km sides and constituted of ten million antennas, i.e., one every 3 m [5]. For simplicity, the beam is approximated by a Gaussian whose full width at half maximum is fixed to $\theta_{\text{fw}} = 0.89\lambda/D$ to match the actual square aperture. In terms of multipole moments, defining

$$\ell_b \equiv \frac{4\sqrt{\ln 2}}{\theta_{\text{fw}}} \quad (31)$$

the beam function (normalized to unity for $\ell = 0$) reads

$$B_\ell = e^{-\ell(\ell+1)/\ell_b^2}. \quad (32)$$

For a system antenna temperature given by T_{sys} the induced flux density fluctuations of one receptor of collecting area \mathcal{A}_1 have a root mean square given by [81, 82]

$$\delta S_\nu = \frac{2T_{\text{sys}}}{\mathcal{A}_1 \sqrt{t_{\text{exp}} B}}. \quad (33)$$

Here t_{exp} stands for the exposure time, B is the frequency bandwidth and the flux density is related to the brightness temperature by $S_\nu = 2T_b/\mathcal{A}_1$. For aperture synthesis against N_{ant} antennas, these fluctuations are reduced by a factor $\sqrt{N_{\text{ant}}(N_{\text{ant}} - 1)/2} \simeq N_{\text{ant}}/\sqrt{2}$ corresponding to the square root of the number of simultaneous pairwise correlations. As a result, the noise fluctuations in the brightness temperature for an array of area D^2 read

$$\delta T_n = \frac{1}{\sqrt{2}} D^2 \frac{\delta S_\nu}{N_{\text{ant}}} \simeq \frac{T_{\text{sys}}}{f_{\text{cov}} \sqrt{t_{\text{exp}} B}}, \quad (34)$$

up to an order unity factor. The covering factor $f_{\text{cov}} \equiv N_{\text{ant}} \mathcal{A}_1 / D^2 = \mathcal{A}_{\text{eff}} / D^2$. For a sky map, δT_n^2 gives the expected noise variance in each pixel subtending a solid angle $\delta\Omega \simeq (\lambda/D)^2$. The angular noise power is thus given by [83]

$$\delta T_n^2 \delta\Omega \simeq \frac{\lambda^2}{D^2 f_{\text{cov}}^2} \frac{T_{\text{sys}}^2}{B t_{\text{exp}}} = \frac{\lambda^2}{\mathcal{A}_{\text{eff}} f_{\text{cov}}} \frac{T_{\text{sys}}^2}{B t_{\text{exp}}}. \quad (35)$$

Depending on the scanning strategy, a telescope may eventually map a solid angle $\Omega_{\text{sky}} = 4\pi f_{\text{sky}}$ larger than its instantaneous field of view Ω_{fov} . This may be taken into account by normalizing the exposure time by a factor $\Omega_{\text{fov}}/\Omega_{\text{sky}}$ [5]. The angular noise power finally reads

$$C_{\text{sys}} \simeq \frac{\lambda^2}{D^2 f_{\text{cov}}^2} \frac{T_{\text{sys}}^2}{B t_{\text{exp}}} \frac{4\pi f_{\text{sky}}}{\Omega_{\text{fov}}}. \quad (36)$$

It is well known from CMB data analysis that, for uncorrelated signal and noise, the root mean square fluctuations for the angular power spectrum are given by [84, 85]

$$\delta C_\ell = \sqrt{\frac{2}{2\ell+1}} \left(C_\ell + \frac{C_{\text{sys}}}{B_\ell^2} \right). \quad (37)$$

The beam effects can thus be included by defining the noise angular power spectrum to be

$$C_\ell^{\text{noise}} \equiv \frac{C_{\text{sys}}}{B_\ell^2}. \quad (38)$$

These results also apply to the three-dimensional power spectrum. Starting from Eq. (35), the corresponding noise spectrum P^{noise} reads

$$P^{\text{noise}}(\mathbf{k}) \simeq \delta T_n^2 \delta V = C_{\text{sys}} D_A^2 y B, \quad (39)$$

where $\delta V = D_A^2 y \delta \Omega B$ is the comoving volume of the three-dimensional pixel intercepting the solid angle $\delta \Omega$ and for a redshift resolution associated with the bandwidth B [see Eq. (18)]. From Eq. (22), one gets the noise power spectrum in the \mathbf{u} variable

$$P^{\text{noise}}(\mathbf{u}) \simeq \frac{\lambda^2}{D^2 f_{\text{cov}}^2} \frac{T_{\text{sys}}^2}{t_{\text{exp}}} \frac{4\pi f_{\text{sky}}}{\Omega_{\text{fov}}}. \quad (40)$$

Beam effects at small scales can be incorporated by multiplying this expression by $\exp(\mathbf{u}_\perp^2 / \ell_b^2)$.

Finally, ionospheric absorption becomes important for all frequencies approaching the plasma frequency $\nu_p \simeq 12$ MHz such that atmosphere is opaque to 21-cm signal coming from $z \gtrsim 100$. For frequencies $\nu \gg \nu_p$ ($z \ll 100$), the ionospheric absorption coefficient A_{iono} on the flux density can be approximated by [81],

$$10 \log(A_{\text{iono}}) \lesssim 0.5 \left(\frac{100 \text{ MHz}}{\nu} \right)^2. \quad (41)$$

For forecasting, instead of applying this damping directly to the expected signal, we prefer to rescale the noise power by multiplying Eqs. (38) and (40) by A_{iono}^2 .

2. Mock power spectra

The fiducial design considered in the following has a size of $D = 10$ km, with a covering factor of $f_{\text{cov}} = 0.1$ and an exposure time of one year, $t_{\text{exp}} \simeq 3.1 \times 10^7$ s. The system temperature is chosen larger than its typical value, $T_{\text{sys}} = 400$ K, to account for some extra noise. Notice that foregrounds removal is generically scale dependent and cannot be simply accounted by a rescaling of T_{sys} [12, 86, 87]. However, as already mentioned, we are here considering an ideal situation and we do not intend to model effects from foregrounds' residuals. For omniscience, the instantaneous field of view and sky coverage have been chosen equal to the visible sky $\Omega_{\text{sky}} = \Omega_{\text{fov}} = 2\pi$, i.e. $f_{\text{sky}} = 0.5$. In Fig. 5, we have plotted the angular power spectrum expected for such a design at various observation redshifts z .

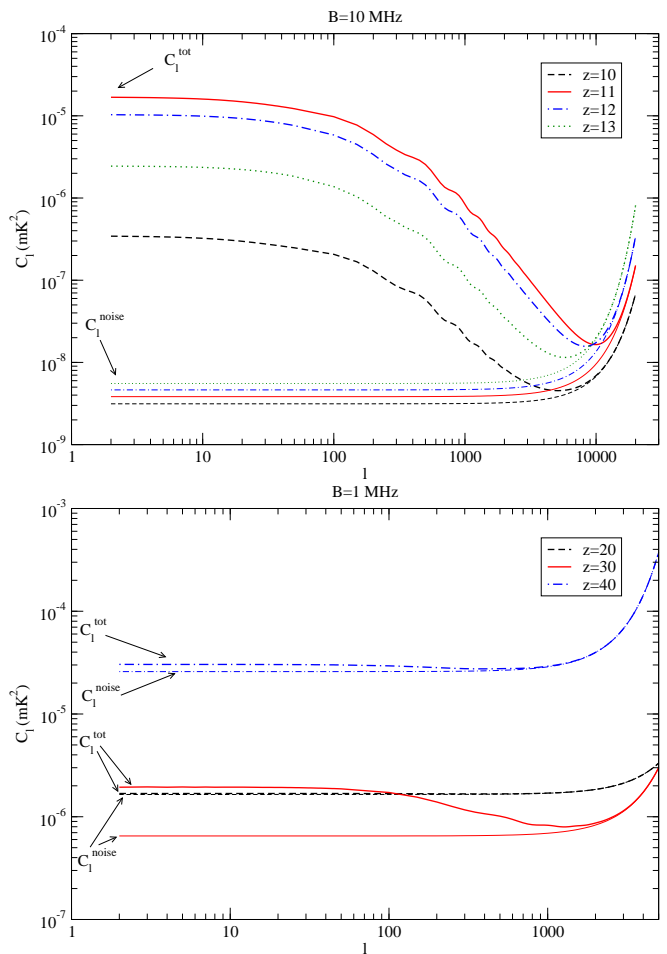


FIG. 5: Mock angular total power spectra $C_\ell + C_\ell^{\text{noise}}$ and C_ℓ^{noise} in mK^2 for various observation redshifts around reionization (top) and at the end of the dark ages (bottom). The cosmological parameters are the ones of Sec. II B ($\tau = 0.088$, $z_{\text{reio}} \simeq 10.5$). The window functions are Gaussian in frequency space with a respective bandwidth of $B = 10$ MHz (top) and $B = 1$ MHz (bottom). The FFTT design is for $D = 10$ km and allows probing the dark ages for $z \lesssim 30$, above which ionospheric absorption damps the signal (see $z = 40$).

III. FORECASTS ON COSMOLOGICAL AND REIONIZATION PARAMETERS

In order to minimize the parameter space dimensions, we consider a simple primordial power spectrum which is a power law with unobservable tensor modes. As shown below, even for vanishing ionization power spectra, FFTT alone does not constrain well the optical depth τ damaging the expected bounds on the background cosmological parameters. As one of the unconstrained parameters is the baryon density $\Omega_b h^2$, the situation can be greatly improved by combining FFTT with CMB data. Taking four redshift slices for the FFTT and Planck-like typical CMB data, we forecast the expected errors on the cosmological parameters and show that all the parame-

ters entering the reionization models can be inferred. At last, the impact of the ionizing power spectra is discussed.

A. Methodology

In the following, we use both Fisher matrix analysis for the three-dimensional power spectra, and MCMC exploration of the parameter space for the angular 21-cm and CMB power spectra. This allows us to discuss how reliable are the expected constraints in presence of degeneracies.

Unless specified, our fiducial cosmological model is the one introduced in Sec. II complemented with a scalar power law primordial power spectrum $\mathcal{P}_s(k) = A_s(k/k_*)^{n_s-1}$, with a pivot scale $k_* = 0.05 \text{ Mpc}^{-1}$. The fiducial spectral index has been fixed to $n_s = 0.973$ and the amplitude to $\ln(10^{10} A_s) = 3.16$. For convenience, we have sampled over the CMB parameter θ , the angular scale of the sound horizon at last scattering, instead of the Hubble parameter H_0 . This facilitates joint CMB and 21-cm analysis discussed later and we have checked that this does not affect significantly the forecasts for 21-cm alone.

1. Fisher matrix analysis

Following the standard approach, given a fiducial set of cosmological and reionization parameters $\{\hat{\lambda}_a\}$, the expected errors on FFTT measurements of the power spectrum $P_{\delta T_b}(\mathbf{u})$ can be evaluated by using the Fisher matrix formalism [71]. Let us assume that we can compute the likelihood \mathcal{L} , i.e. the expected distribution of the data given a certain model. The Fisher matrix approach assumes that the expected behaviour of the likelihood near the maximum is Gaussian such that its curvature alone allows to estimate errors on the parameters. The Fisher information matrix is defined as

$$\mathbf{F}_{ab} = - \left\langle \frac{\partial^2 \ln \mathcal{L}}{\partial \lambda_a \partial \lambda_b} \right\rangle, \quad (42)$$

where the brackets denote an ensemble average. When all the parameters are estimated simultaneously, the marginalized error on a given parameter reads $\sigma_{\lambda_a} \geq \sqrt{(\mathbf{F}^{-1})_{aa}}$. The Cramér-Rao inequality (“ \geq ”) emphasizes the fact that the Fisher matrix approach always gives a local optimistic estimate of the errors. It becomes an equality when the likelihood is a Gaussian around its maximum. In the following, we estimate the expected variance on the measured parameters λ_a from the diagonal elements of the covariance matrix, i.e. from the inverse Fisher matrix elements

$$\langle \delta \lambda_a^2 \rangle = (\mathbf{F}^{-1})_{aa}. \quad (43)$$

For the purpose of the Fisher matrix analysis, as already mentioned in Sec. II A 3, one can divide the sky

into small patches for which the flat sky approximation is valid. Given an angular patch Θ and a frequency bin of size F , the probed comoving volume is

$$V = \Theta^2 D_A^2 F y. \quad (44)$$

Following [44], one can consider step sizes in the dual \mathbf{u} space as follows:

$$\delta u_{\perp} = \frac{2\pi}{\Theta}, \quad \delta u_{\parallel} = \frac{2\pi}{F}, \quad (45)$$

where Θ is taken to be lower than typically 1 rad and F is set by the frequency size of the redshift bin. Assuming that $P_{\delta T_b}(\mathbf{u})$ is Gaussian distributed, we can approximate the Fisher matrix by

$$\mathbf{F}_{ab} = \frac{1}{2} \sum_{u_{\parallel}, u_{\perp}} \frac{N_c}{[P_{\delta T_b}(\mathbf{u}) + P^{\text{noise}}]^2} \frac{\partial P_{\delta T_b}(\mathbf{u})}{\partial \lambda_a} \frac{\partial P_{\delta T_b}(\mathbf{u})}{\partial \lambda_b}, \quad (46)$$

where

$$N_c = \frac{4\pi f_{\text{sky}}}{\Theta^2} 2\pi k_{\perp} \delta k_{\perp} \delta k_{\parallel} \frac{V}{(2\pi)^3}, \quad (47)$$

is the number of independent cells probed⁴ for a given value of \mathbf{k} , or equivalently of \mathbf{u} . Notice that given Eqs. (44) and (45), N_c reduces to

$$N_c = \frac{4\pi f_{\text{sky}}}{\Theta^2} \frac{2\pi k_{\perp}}{\delta k_{\perp}}. \quad (48)$$

In the following, we will be interested in comparing the results of the Fisher analysis on the three-dimensional power spectrum $P_{\delta T_b}(\mathbf{u})$ to the results of a MCMC analysis which makes use of the angular power spectrum C_{ℓ} . From our experimental design, the measured 21-cm power spectrum is, however, convolved in frequency by a Gaussian window function of width B . As the result, and unless specified, we will also compute the Fisher matrices of Eq. (46) from the three-dimensional power spectrum at $k_{\parallel} = 0$ after a convolution with the same Gaussian window function. Compared to Ref. [44], this allows us to consider larger redshift bins, and thus larger bandwidths, in which the power spectrum and background quantities are allowed to vary. In Ref. [44], the FFTT was assumed to have a small bandwidth of $B \simeq 0.15 \text{ MHz}$. Around each observation redshift, the signal on a bin of size $\delta z \simeq 0.5$ is expanded in Fourier modes u_{\parallel} , up to $u_{\parallel}^{\text{max}} = 2\pi/B$. Within our approach, this Fourier expansion is now replaced by a convolution of the signal with the frequency window function associated with the mean redshift of observation. Combining multiple redshifts is still done by adding up their respective Fisher matrices.

⁴ The factor 1/2 in Eq. (46) takes into account the fact that \vec{k} and $-\vec{k}$ are not independent.

Let us stress that when the bandwidth is small enough, there is no need for the convolution. Summing the Fisher on u_{\parallel} running on positive and negative values with $|u_{\parallel}^{\max}|$ set by the frequency resolution of the experiment, i.e. the bandwidth B , gives the same result than subdividing the redshift bin in an identical number of slices to the number of parallel modes. We have cross-checked our method by using the FFTT specifications and reionization model of Ref. [44], for which we recover the same results, in the small bandwidth limit.

Concerning the transverse modes, since the volume of the experiment is finite, only a discrete number of modes is theoretically accessible to the analysis. In Eq. (46), the sum over u_{\perp} runs over positive values from $u_{\perp}^{\min} = 2\pi/\Theta$, to $u_{\perp}^{\max} \simeq 2\pi D/\lambda$, the angular resolution being set by the longest baseline of the experiment, D .

Finally, let us also mention that when constructing the Fisher matrix, one has to pay special attention to the numerical accuracy at which the power spectrum derivatives have been estimated. Indeed, the evolution of the 21-cm power spectrum with the cosmological parameters can be highly non linear and is furthermore redshift dependent. As discussed in Ref. [88], one has to find a good compromise between small step sizes in the numerical evaluation of the derivatives and the appearance of numerical noise. For each parameter, a step size corresponding roughly to 2% of the fiducial values was found to be a good compromise. For each redshift, the power spectrum needs to be calculated for a large number of wavelength modes (typically 3000), and in order to spare computing time, it has been interpolated using 20 k values per unit logarithmic interval. The derivatives have been evaluated by means of a four-point method for well-behaved parameters whereas for n_s , A_s , plus the nuisance reionization parameters N_{ii} , R_{ii} , α_{ii} , γ_{ii} , N_{ib} , R_{ib} and α_{ib} , the derivatives have been determined analytically. Finally, to keep the numerical noise under control, the transfer functions have been computed using high precision settings within CAMB.

2. Markov Chain Monte Carlo

From the mock data associated with the FFTT design of Sec. II C, forecasts can be derived through MCMC exploration of the parameter space provided one specifies the likelihood. As for the Fisher analysis, the mock data $\{\hat{C}_{\ell}\}$ are assumed to be associated with a set of fiducial parameters $\{\hat{\lambda}_a\}$. For a full sky analysis, one can show that the sampling distribution followed by the C_{ℓ} is a gamma distribution [89]. For a cut sky, with an isotropic beam and noise, one can use the approximated likelihood [90, 91]

$$-2 \ln \mathcal{L}(D_{\ell}|\hat{D}_{\ell}) = \sum_{\ell} f_{\text{sky}}(2\ell + 1) \left(\frac{\hat{D}_{\ell}}{D_{\ell}} + \ln \frac{D_{\ell}}{\hat{D}_{\ell}} - 1 \right). \quad (49)$$

Here D_{ℓ} denotes the theoretical angular power spectrum, plus noise, i.e.

$$D_{\ell} = C_{\ell} + \frac{C_{\ell}^{\text{noise}}}{B_{\ell}^2}, \quad (50)$$

associated with any tested set of parameters $\{\lambda_a\}$. The same equation is used to define the \hat{D}_{ℓ} from the fiducial \hat{C}_{ℓ} . From our modified version of the CAMB code, and FFTT specifications, the D_{ℓ} can be computed for any input value of the cosmological and reionization parameters $\{\lambda_a\}$. Using MCMC sampling with the likelihood of Eq. (49) allows to extract their posterior probability distribution for a given fiducial model $\{\hat{\lambda}_a\}$. In the following, we have used a modified version of the public code CosmoMC coupled with our modified CAMB code [74].

B. Single redshift from dark ages

In this section, the above-described MCMC analysis is applied to one dark ages redshift $z = 30$. As discussed in Sec. II C, the 21 cm physics during dark ages is free of reionization uncertainties, up to the optical depth. Within our design, it has a low signal-to-noise ratio whose only interest is to exacerbate the degeneracies induced by the optical depth into the other cosmological parameters. In Fig. 6, we have plotted the marginalized probability distribution on the cosmological parameters for the same reionization model used for CMB data analysis, namely only τ (or z_{reio}) is varying.

Both the primordial power spectrum amplitude A_s and τ enter into the amplitude of the 21-cm signal and one expects them to be degenerated. As Figs. 6 and 7 show, these parameters are in fact mostly degenerated with $\Omega_b h^2$. This is expected because, as can be seen in Eq. (10), the baryon density also enters into the overall amplitude of the signal. Moreover, even for a fixed τ , and fixed observation redshift z , τ_c still inherits extra dependencies on the other cosmological parameters from their influence on the background evolution. As a result, all parameters end up being more or less contaminated by the reionization parameter τ , which seriously damages the expected constraints compared to a situation in which τ would be perfectly known. The notable exception concerns the spectral index n_s , simply because the number of modes accessible to the FFTT is large enough to detect its effect over background degeneracies, these ones affecting all modes in a smoother way. Nevertheless, the forecasts on n_s do not compete with CMB bounds. Let us stress that we have used only one redshift slice to emphasize the above-mentioned degeneracies and one could add other redshifts to improve the constraints. However, for the dark ages, the signal dominates over the noise only around $z \simeq 30$ (see Fig. 5) and the above degeneracies still remain. The situation is better at EoR.

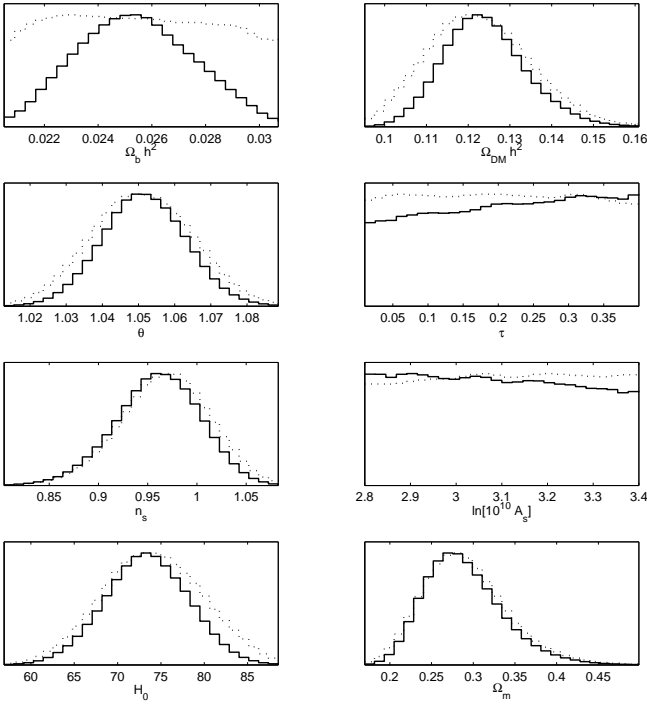


FIG. 6: Expected marginalized posterior probability distributions (solid) and mean likelihood (dotted) for 10 km FFTT data alone, at $z = 30$ (dark ages). The total optical depth τ , primordial amplitude A_s , baryon density $\Omega_b h^2$ are completely degenerated and not constrained (see text and Fig. 7).

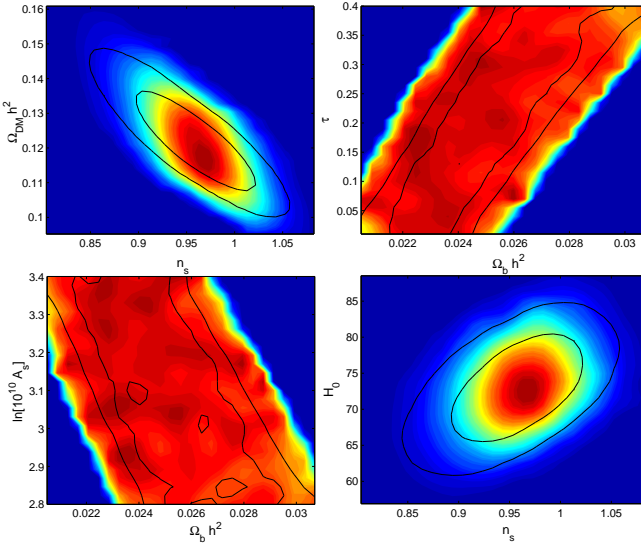


FIG. 7: One- and two-sigma confidence interval of the two-dimensional marginalized posterior probability distributions (solid lines) for a 10 km FFTT design at $z = 30$. The shading traces the two-dimensional mean likelihood.

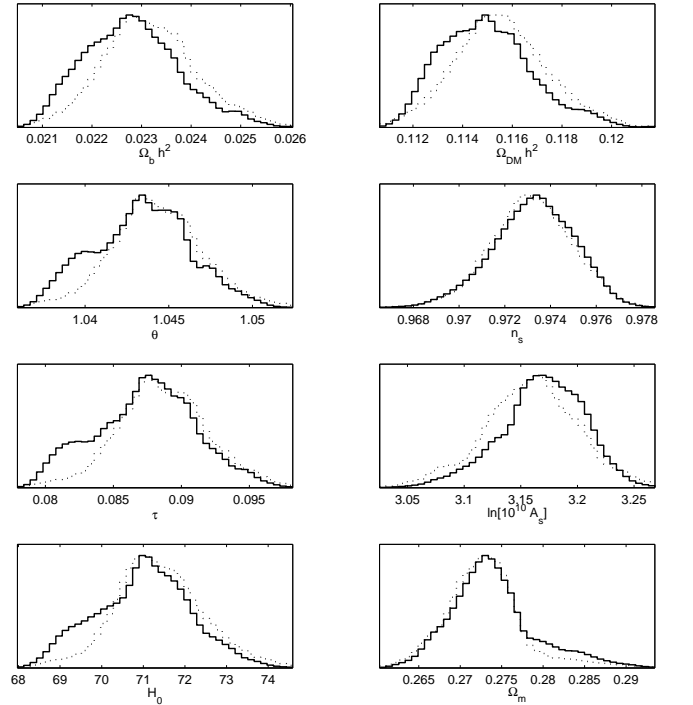


FIG. 8: Expected marginalized posterior probability distributions (solid) and mean likelihood (dotted) from a single redshift observation at $z = 11$ (reionization). The non-Gaussian posteriors and “shoulders” apparent for some parameters comes from the large correlations induced by τ (see Fig. 9).

C. Epoch of Reionization

The fiducial model is unchanged but the observation redshifts now probe the beginning of the EoR.

1. Optical depth induced degeneracies for one redshift

As for the dark ages, we have first performed our analysis for a single redshift slice $z = 11$, close to the maximum signal-to-noise ratio of the 10 km FFTT and sampled at $B = 10$ MHz. In an optimal situation, the ionizing power spectrum can be switched off and the background reionization model has only τ varying.

The MCMC forecasts are represented in Figs. 8 and 9 as one- and two-dimensional posterior distributions.

As for the dark ages, the degeneracies induced by τ are still present and propagate to the other parameters as well. However, τ , A_s and $\Omega_b h^2$ are now constrained. This comes from the signal to noise ratio at $z = 11$ which is much larger than for the dark ages, but also from the stronger effects induced by τ which makes the degeneracies nonlinear. As seen in Fig. 8, the marginalized probability are non-Gaussian and distorted by their correlations. This is particularly visible in the two-dimensional

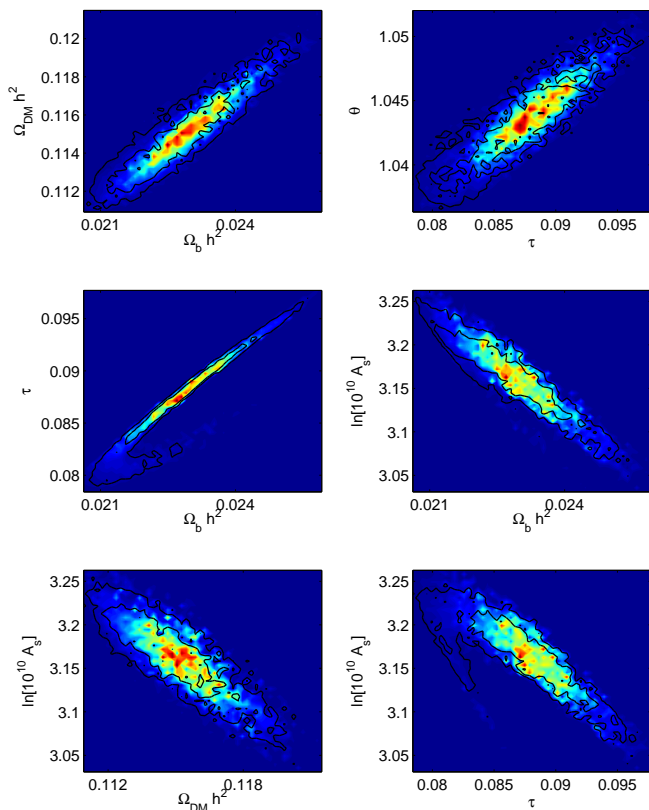


FIG. 9: Two-dimensional posteriors for a single observation redshift at $z = 11$. The solid lines represent the one and two-sigma confidence interval while the shading traces the two-dimensional mean likelihood. Notice the strong degeneracies induced by τ which boost the expected variance on $\Omega_b h^2$ for instance.

likelihood in the plane $(\tau, \Omega_b h^2)$ (see Fig. 9). Compared to the dark ages, varying τ affects the background signal amplitude at EoR through x_H and T_s . Compared to previous works derived with Fisher matrix methods, our forecasts are slightly less optimistic, but as it should be clear from Fig. 9, not including τ reduces the expected error bars on various other cosmological parameters (see below). The need of breaking degeneracies clearly suggests the inclusion of additional data, either 21-cm from other redshift slices, or CMB data.

We have also performed a Fisher matrix analysis under the same model and experimental hypothesis, both on the convolved and nonconvolved 21-cm three-dimensional power spectra. Our results are reported in Table II. Without convolution, the strong degeneracy between τ and $\ln A_s$ leads to a ill-conditioned Fisher matrix that can be hardly inverted. This can therefore induce important numerical errors in the forecasts. Physically, this means that one combination of parameters is completely unconstrained from the Fisher point of view: the Gaussian approximation would predict some flat directions for the likelihood. In such a situation, Fisher results can still

be derived provided the problematic parameters are artificially removed to recover a well-behaved matrix.

The convolution with the frequency window function reduces the degeneracy between the parameters τ and $\ln A_s$ but still does not cure the existence of flat directions. In Table II, we have reported the forecasts when removing either $\ln A_s$ or τ from the Fisher analysis. Forecast on the other parameters can be slightly overpessimistic compared to the MCMC. This is expected because, even with the convolution included, the Fisher results still approximate any degeneracies as linear. Figure 9 shows that this is clearly not the case, as for instance in the plane $(\Omega_b h^2, \tau)$ where the two-sigma contour is actually multivalued. Let us notice that removing τ in the Fisher matrix yields an order of magnitude wrong prediction for $\ln A_s$, whereas removing $\ln A_s$ gives a standard deviation for τ compatible with the MCMC result (see Table II). These observations reinforce the need of MCMC methods as soon as some degeneracies are not under control.

	$\Omega_b h^2$	$\Omega_{\text{dm}} h^2$	n_s
M	9.5×10^{-4}	1.8×10^{-3}	1.8×10^{-3}
F (no conv.)	7.9×10^{-4}	1.5×10^{-3}	1.3×10^{-3}
F (conv.)	9.2×10^{-4}	1.9×10^{-3}	1.7×10^{-3}
F (no conv.)	8.0×10^{-4}	1.6×10^{-3}	1.3×10^{-3}
F (conv.)	9.8×10^{-4}	2.0×10^{-3}	1.8×10^{-3}
	τ	$\ln(10^{10} A_s)$	H_0
M	3.7×10^{-3}	3.7×10^{-2}	1.1
F (no conv.)	3.0×10^{-3}	-	0.9
F (conv.)	4.0×10^{-3}	-	1.0
F (no conv.)	-	0.24	0.9
F (no conv.)	-	0.21	1.0

TABLE II: Standard deviations on cosmological parameters for FFTT-only single redshift measurements at $z = 11$ from both MCMC method (M) and Fisher matrix analysis (F). The Fisher results are given for both the nonconvolved and convolved power spectrum and by removing from the analysis one of the strongly degenerated parameters, either τ or $\ln(10^{10} A_s)$.

2. Multiredshifts tomography

Still with vanishing ionizing power spectra and a reionization model having only τ varying, we can reduce the FFTT degeneracies by adding extra redshift slices. As before, we have performed MCMC analysis on the full sky mock data and Fisher matrix methods on the associated 21-cm power spectrum.

In Figs. 10 and 11 we have represented the MCMC posteriors obtained by considering two redshift slices, $z = 11, z = 12$, and four redshift slices $z = 10, z = 11, z = 12, z = 13$. The telescope is, as before, the 10 km FFTT with $B = 10$ MHz and all other parameters are the same.

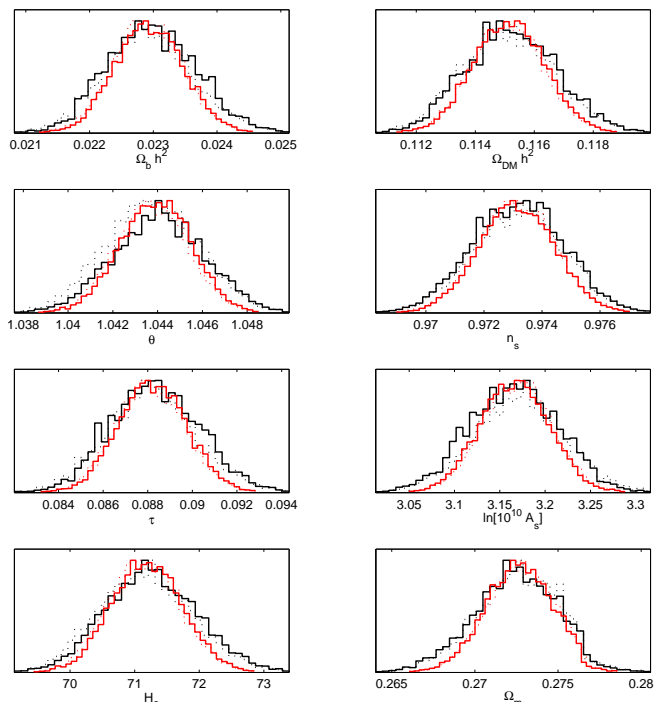


FIG. 10: Marginalized posteriors (solid) and mean likelihood (dotted) from two and four observation redshifts at reionization. The black outer curves are for two redshift slices $z = 11$, $z = 12$ while the red inner ones for four redshift $z = 10$, $z = 11$, $z = 12$ and $z = 13$ (see also Fig. 11).

Compared to $z = 11$ alone, the degeneracies have been reduced. In fact, one can check that a data analysis performed at $z = 12$ alone would produce similar posteriors as those obtained for $z = 11$ with, however, slightly different degeneracy directions in the parameter space. Combining both can be viewed as keeping only the intercepting probability contours of each redshift slice. For τ , the standard deviation ends up being reduced by almost a factor of two, while this is not as significant for the other parameters. Their posteriors do no longer exhibit “shoulders” or evident non-Gaussian shapes, however Fig. 11 shows that they still are correlated along some peculiar directions. Adding more redshifts again improves the situation, but the correlation trend does not disappear due to the common physical origin of all 21-cm signals at reionization. The inner red curves in Fig 10 and Fig 11 are the same analysis performed on four redshift slices, scanning the whole reionization duration: $z = 10$, $z = 11$, $z = 12$ and $z = 13$. The standard deviations are slightly reduced, but less than the expected $\sqrt{2}$ factor because both $z = 10$ and $z = 13$ correspond to a low emission signal (see Fig. 5). Let us notice that a bandwidth $B = 10$ MHz corresponds in term of redshift to a width $\delta z \simeq 1$ (at $z = 11$). Requiring more redshift slices at reionization would therefore also demands a smaller bandwidth.

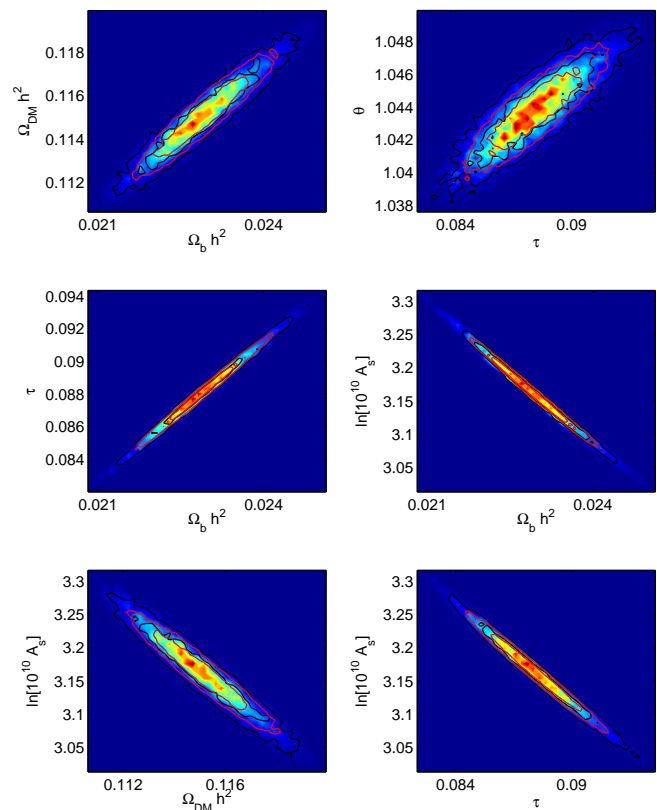


FIG. 11: Two-dimensional posteriors obtained by combining the FFTT data from multiple redshift slices. The shading traces the mean likelihood associated with the combination of two redshifts $z = 11$ and $z = 12$. The black largest contours are the associated one- and two-sigma confidence intervals whereas the smaller gray contours are those associated with combined data for four redshifts ($z = 10$, $z = 11$, $z = 12$ and $z = 13$). The degeneracies induced by τ are accordingly reduced.

Let us turn now to the Fisher analysis. The forecasts for the four redshifts $z = 10$, $z = 11$, $z = 12$ and $z = 13$ and the convolved 21-cm power spectrum are given in Table III. Our results agree relatively well with those from the MCMC method, even if the forecasts are found to be about 20% more stringent with the Fisher matrix analysis. We have also checked that the degeneracy directions between parameters were matching the ones obtained from the MCMC and represented in Fig. 11.

3. Adding Planck-like CMB data

The previous results call for the incorporation of other cosmological data having different correlations. In the following, we incorporate CMB data and consider a typical Planck-like experiment. For our purpose, we have generated mock CMB data exactly as described in Sec. II C, but for a full sky CMB experiment ($f_{\text{sky}} = 1$), with a Gaussian beam of resolution $\theta_{\text{FW}} = 7'$ and a con-

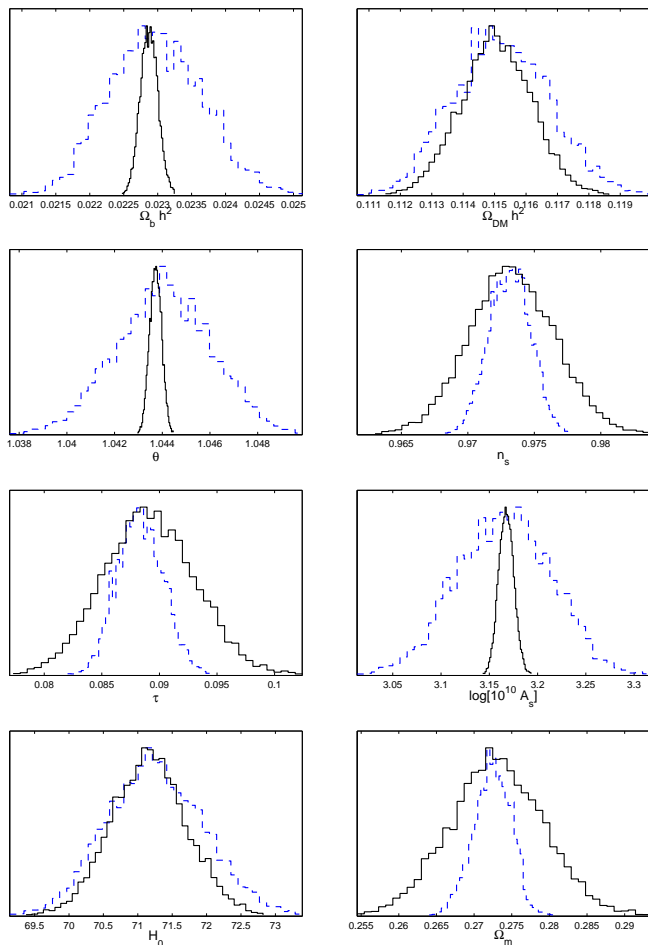


FIG. 12: Typical marginalized posterior distributions for a Planck-like CMB experiment (black solid lines). The dashed blue curves are the two redshift forecasts for FFTT (same as in Fig. 10).

stant noise for each pixel given by $\langle \delta T_n^2 \rangle = 2 \times 10^{-4} \mu K^2$ (twice for the E -mode polarization) [92, 93]. Performing a MCMC analysis with Planck-like mock data alone, and for the same fiducial parameter values, yields the posterior plotted in Fig. 12. To ease the comparison, we have reported on the same figure the two redshifts' FFTT forecasts.

CMB data give much stronger constraints on $\Omega_b h^2$, A_s and θ than the considered 10 km FFTT design. This is expected because the overall amplitude of the CMB signal depends mainly on A_s and not $\Omega_b h^2$ contrary to the 21-cm brightness. Concerning θ , it is an optimal parameter for CMB by design whereas H_0 shows similar posteriors for both CMB and 21 cm. Interestingly, the spectral index is, by a factor of two, more constrained by 21-cm. One can also check in Fig. 8 that this would also be the case with only one observation redshift at $z = 11$. This is again due to the huge level arm provided by the FFTT resolution on the power spectrum shape. More-

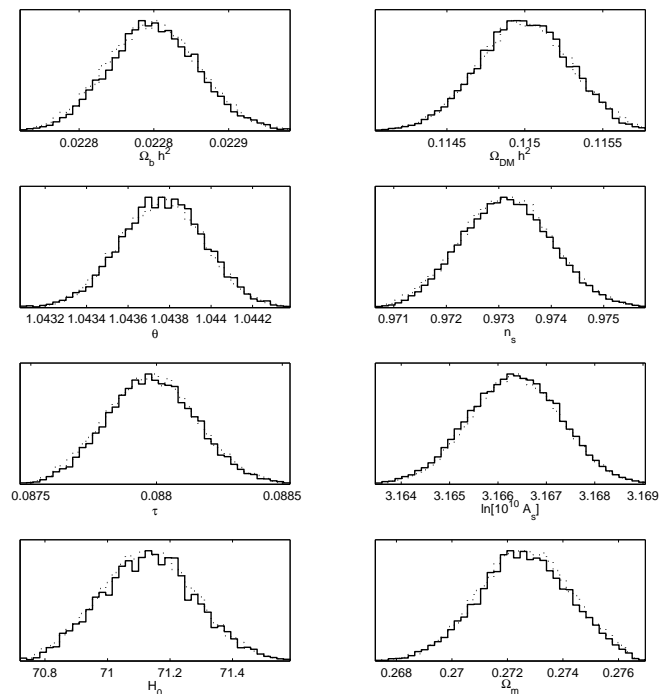


FIG. 13: Marginalized posteriors from the combination of the FFTT four redshifts data ($z = 10$, $z = 11$, $z = 12$ and $z = 13$) with Planck-like CMB data. The reduced variance on $\Omega_b h^2$ coming from CMB data kills most of the degeneracies associated with the 21-cm signal. Four redshifts' FFTT without CMB is represented in Fig. 10.

over, Fig. 12 shows that, in spite of the degeneracies, the marginalized posterior for τ remains sharper for FFTT than for CMB. This could wrongly suggest that adding CMB data may not help to improve the FFTT constraints over τ . However, τ is mostly correlated with $\Omega_b h^2$ which is well bounded by CMB alone. As a result, CMB data are expected to indirectly improve the FFTT accuracy on τ .

We have checked that this is indeed the case by performing a MCMC analysis based on Planck-like CMB data together with the four redshifts' FFTT data. The resulting posterior probability distributions are represented in Fig. 13. The expected standard deviation on τ is reduced by an order of magnitude. In Fig. 14, the two-dimensional posterior confirms that such an improvement comes from the significant reduction in the variance of $\Omega_b h^2$ due to CMB data. For comparison, we have also reported in this figure the one- and two-sigma confidence intervals for the four redshifts' FFTT alone (see Fig. 11). For some parameters, the improvement is such that they may lie outside the displayed plane.

The forecasts derived from the Fisher matrix are reported in Table III. As the degeneracies are even more reduced by the inclusion of CMB data, the Fisher results agree well with those from the MCMC analysis. The degeneracy axes associated with one-sigma ellipses

Data	Method	$\Omega_b h^2$	$\Omega_{\text{dm}} h^2$	θ	n_s	τ	$\ln(10^{10} A_s)$	H_0
FFTT alone	M	5.4×10^{-4}	1.2×10^{-3}	1.6×10^{-3}	1.3×10^{-3}	1.5×10^{-3}	3.8×10^{-2}	0.55
	F	4.2×10^{-4}	9.5×10^{-4}	1.3×10^{-3}	1.0×10^{-3}	1.2×10^{-3}	2.9×10^{-2}	0.45
	F ($B = 0.1$ MHz, no conv.)	2.3×10^{-5}	1.6×10^{-4}	1.4×10^{-4}	1.7×10^{-4}	4.9×10^{-5}	2.3×10^{-3}	4.9×10^{-2}
FFTT + CMB	M	3.0×10^{-5}	2.9×10^{-4}	2.0×10^{-4}	8.6×10^{-4}	1.8×10^{-4}	9.5×10^{-4}	0.15
	F	2.8×10^{-5}	2.6×10^{-4}	2.2×10^{-4}	7.2×10^{-4}	1.6×10^{-4}	9.0×10^{-4}	0.13
	F ($B = 0.1$ MHz, no conv.)	8.1×10^{-6}	3.9×10^{-5}	8.3×10^{-5}	5.7×10^{-5}	3.6×10^{-5}	3.4×10^{-4}	1.2×10^{-2}

TABLE III: Expected standard deviations for the basic parameters in the case of four redshifts' FFTT alone and complemented with Planck-like CMB data. The reionization model has only one varying parameter τ , the ionizing power spectra are assumed to be negligible (for the MCMC method, H_0 is a derived parameter and is reported in the last column). The method refers to either MCMC (M) full sky analysis or the Fisher matrix (F) on the 21cm three-dimensional power spectrum (with convolution). The third and sixth lines show the Fisher results (without convolution) in the small bandwidth limit $B = 0.1$ MHz, with $\delta z = 0.5$, for which 40 u_{\parallel} modes would be accessible.

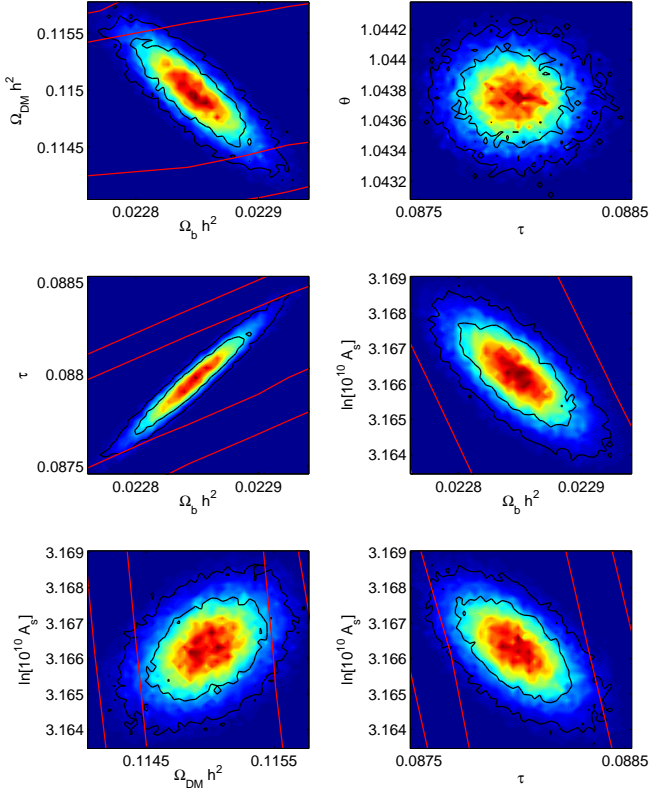


FIG. 14: Two-dimensional marginalized probability distribution for the combined four redshifts' FFTT and Planck-like CMB data. The inner black solid lines are the one- and two-sigma confidence intervals, the shading traces the mean likelihood. The outer red lines are the one- and two-sigma confidence intervals for four redshifts' FFTT data alone. The precise determination of $\Omega_b h^2$ from CMB strongly reduces the $(\tau, \Omega_b h^2)$ correlations associated with the 21-cm signal.

are also found to be in agreement with the MCMC two-dimensional posteriors (not represented).

As the Fisher matrix approach can be trusted in this regime, one can discuss the effect of increasing the number of modes by reducing the bandwidth. For $B =$

0.1 MHz, still using the same four mean redshifts, with a bin size of $\delta z = 0.5$, it is no longer necessary to include the convolution. In that case, there are about 40 parallel modes accessible along the line-of-sight, up to a nonlinear cutoff fixed at $k_{\parallel} = 2 \text{ Mpc}^{-1}$ [44] (see Table III).

In the following sections, we relax some of the reionization assumptions and consider that duration and maximal spin temperature are no longer known.

4. Spin temperature evolution and reionization duration

The reionization model of the previous sections involved a unique varying parameter τ . One may now wonder how the forecasts are affected by the reionization duration Δ_z and the maximal spin temperature T_s^{max} . Again, the fiducial model is unchanged, i.e., has $\hat{\Delta}_z = 0.5$ and $\hat{T}_s^{\text{max}} = 10000 \text{ K}$.

Figures 15 and 16 show the probability distributions obtained from the MCMC exploration based on the same data, i.e. four redshifts' FFTT plus CMB Planck-like data. The two additional reionization parameters are very well constrained. Even for the large chosen fiducial value \hat{T}_s^{max} , the expected standard deviation does not exceed 20 K. This directly comes from the FFTT tomography. Along the four redshifts probed, the 21cm signal is very sensitive to the neutral hydrogen fraction $x_{\text{H}}(z)$ and the value of $T_s(z)$ thereby providing accurate forecasts for the related parameters. As visible in Fig. 16, T_s^{max} is slightly correlated with Δ_z but this is expected in view of our smooth reionization model (see Fig. 1). Increasing T_s^{max} at a given redshift mimics a reduction in Δ_z . The correlations remain under control because we use more than one redshift. These results also suggest that taking the asymptotic limit $T_s \rightarrow \infty$ at reionization is not always justified and throws away some potentially available information.

We find that the Fisher matrix analysis, with convolution included, does not resolve completely the degeneracy between T_s^{max} and Δ_z thereby rendering the Fisher matrix singular. As before, one needs to remove the incriminated flat directions, and we had to pull out T_s^{max} from

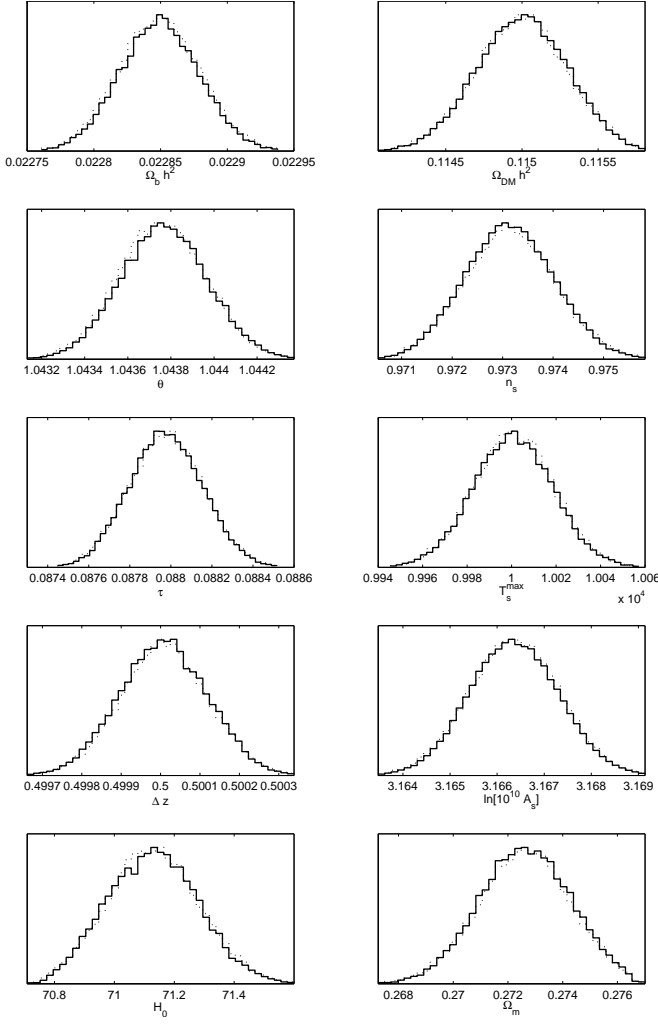


FIG. 15: Posterior probability distributions from combined FFTT four redshifts and Planck-like CMB data. The background reionization model has three varying parameters, τ , Δ_z and T_s^{\max} , all well reconstructed.

	$\Omega_b h^2$	$\Omega_{\text{dm}} h^2$	n_s	H_0
M	3.0×10^{-5}	2.9×10^{-4}	8.8×10^{-4}	0.15
F	2.9×10^{-4}	2.6×10^{-4}	7.4×10^{-4}	0.14
	τ	$\ln(10^{10} A_s)$	$T_s^{\max}(\text{K})$	Δ_z
M	1.8×10^{-4}	9.5×10^{-4}	18	1.1×10^{-4}
F	1.6×10^{-4}	9.4×10^{-4}	-	2.7×10^{-4}

TABLE IV: Standard deviations for the combined four redshifts' FFTT and CMB for a reionization model with three varying parameters τ , Δ_z and T_s^{\max} . There is no loss of accuracy compared to Table. III showing that redshift tomography allows the complete reconstruction of the reionization parameters. The labels ‘‘M’’ and ‘‘F’’ respectively refer to MCMC and Fisher matrix analysis (with convolution). The Fisher matrix has to be regularized at the expense of losing information by removing one of the degenerated parameters, here T_s^{\max} .

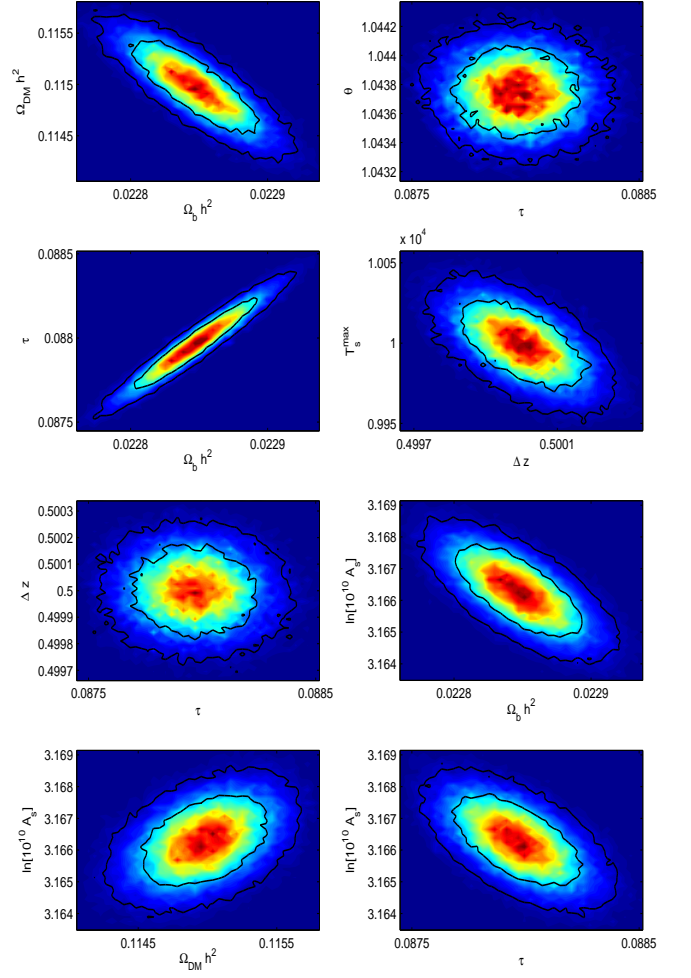


FIG. 16: Two-dimensional posterior probability distributions associated with the combined FFTT four redshifts and Planck-like CMB data (see also Fig. 15). The background reionization model parameters, τ , Δ_z and T_s^{\max} are weakly correlated and well reconstructed.

the analysis⁵. In this case, the predicted standard deviations are in good agreement with the MCMC results, whereas larger differences between the two methods appear for Δ_z . This is again not surprising because those parameters are correlated (see Fig. 16).

In the next section, we relax the assumption that the ionizing power spectra are negligible and consider their impact on the model parameter forecasts.

⁵ Removing Δ_z still yields an almost singular matrix generating spurious numerical errors at inversion.

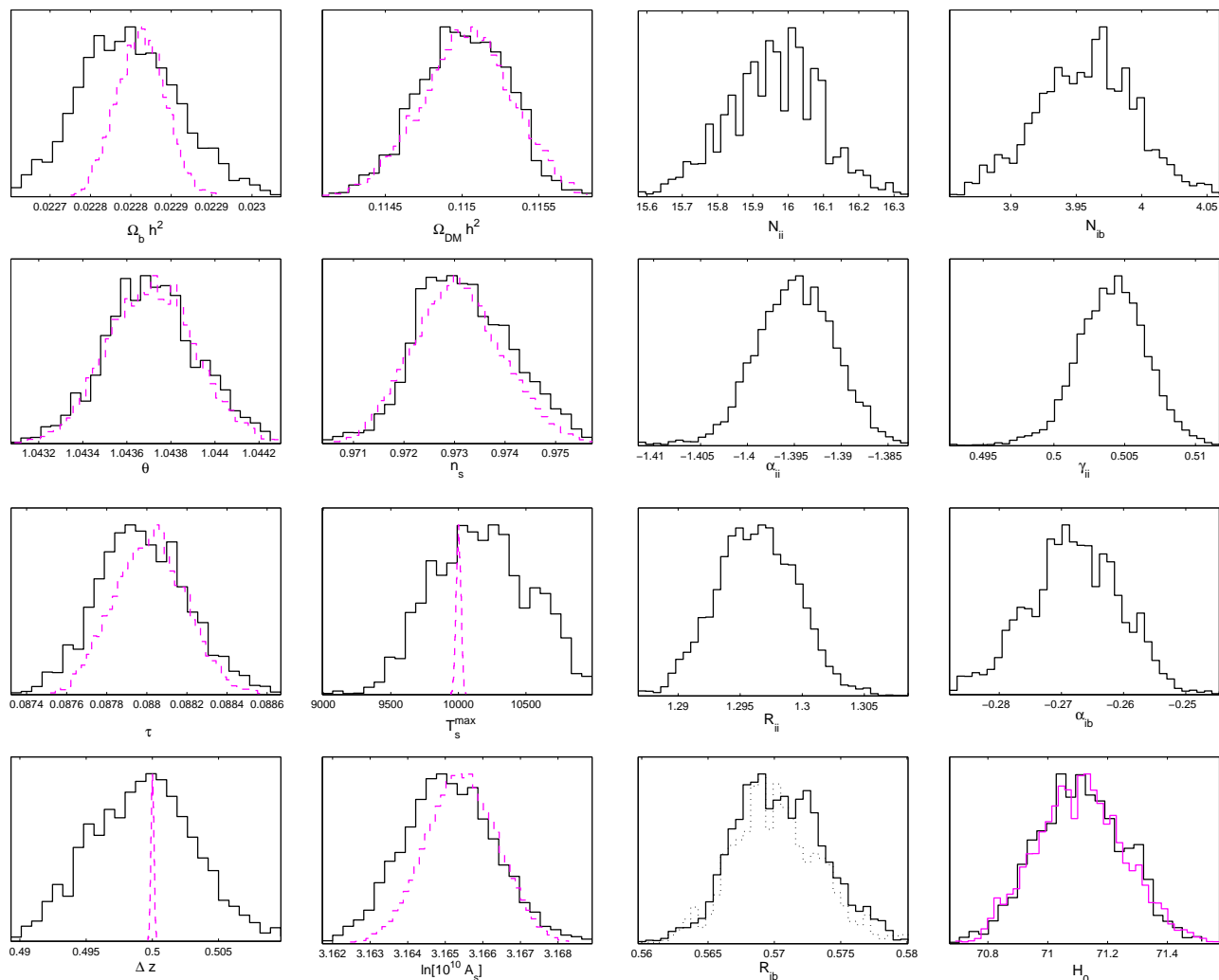


FIG. 17: Posterior probability distributions in presence of the ionizing power spectra. The background reionization model has three varying parameters, τ , Δ_z and T_s^{\max} while the ionizing spectra involves seven nuisance parameters N_{ii} , α_{ii} , γ_{ii} , R_{ii} , N_{ib} , α_{ib} and R_{ib} . The posteriors of Fig. 15 have been reported as dashed curves to ease comparison.

5. Nuisance ionization power spectra

As in Ref. [44], we consider a less ideal situation in which the ionizing sources affect the 21-cm perturbations by switching on the extra power spectra P_{ib} , P_{ii} of Eq. (15). According to the discussion of Sec. IIB 2, the redshift evolution of our toy ionizing spectra is completely encoded into $x_H(z)$ and $x_i(z)$; as in Eq. (16). In total, this adds seven nuisance parameters to the analysis, namely N_{ii} , R_{ii} , α_{ii} , γ_{ii} , N_{ib} , R_{ib} and α_{ib} . In a more realistic situation, the ionizing spectra may involve more parameters and have certainly more complicated shapes, but their redshift evolution should still be correlated with the background reionization history.

Using again the four redshifts' FFTT plus Planck-like CMB data, we have plotted in Fig. 17 and 18 the resulting marginalized probability distributions when the ionizing spectra are switched on. The fiducial values of

all parameters are the same as before while the seven nuisance parameters have been fixed to the fiducial values of Table I.

The most important result is that the posteriors for the cosmological parameters are almost unchanged compared to Fig. 15 thereby confirming that the presence of nuisance ionizing spectra should not prevent cosmological parameter estimation [44]. The expected standard deviations have been reported in Table V, and up to an increase for $\Omega_b h^2$ and τ , the bounds of all the other cosmological parameters are identical to the ones of Table. IV. Let us stress again that this result incorporates marginalization over all background reionization histories accessible within our model.

The situation is different for the background reionization parameters. The standard deviation associated with the posteriors of Δ_z and T_s^{\max} is more than one order of magnitude larger than those obtained without ionizing

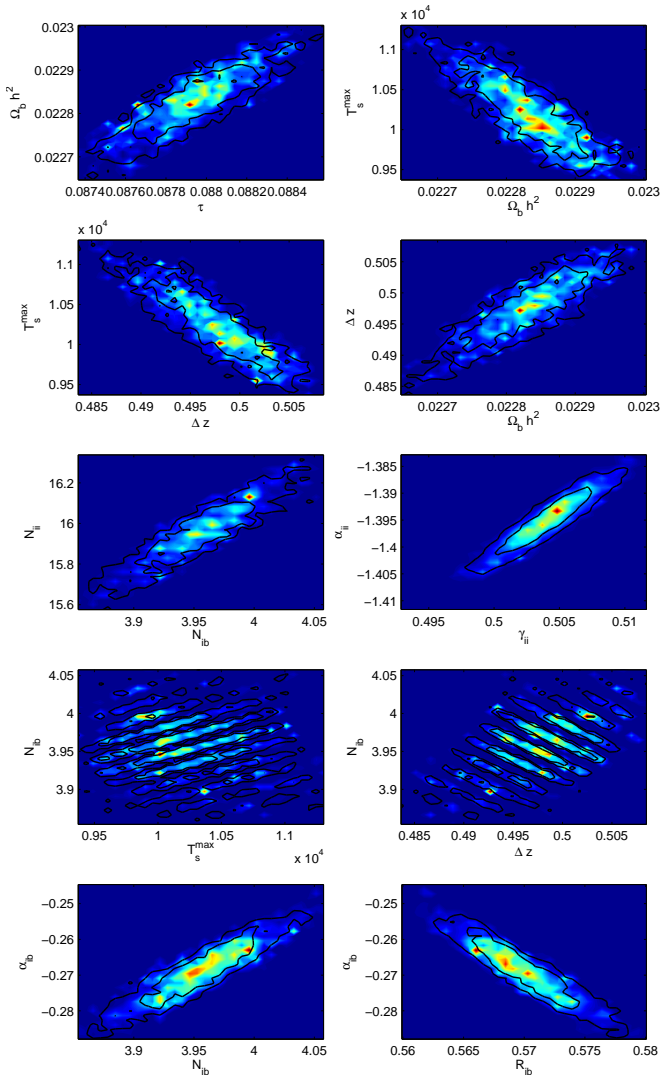


FIG. 18: Two-dimensional posterior probability distributions in presence of the ionizing power spectra. The correlations induced by the nuisance parameter N_{ib} severely damages the expected constraints on the background reionization parameters Δ_z and T_s^{max} . The multivalued confidence intervals are the results of the acoustic oscillations (see text).

spectra. As can be seen in Fig. 18, the two-dimensional posteriors exhibit strong correlations between the nuisance parameters and Δ_z and T_s^{max} . This can be understood from Fig. 4. Around the redshift of maximum sensitivity ($z \simeq 11$), the total ionizing spectra is dominated by P_{ib} . Its amplitude N_{ib} therefore affects the overall observable signal and should therefore correlate to all the other amplitude related parameters. However, since we use CMB data, the parameters $\Omega_b h^2$ and τ are relatively well constrained, independently of the values of N_{ib} . They are therefore weakly affected by these new correlations. It remains the neutral fraction x_{H} , which is precisely given by the background reionization history, i.e. by the value of Δ_z and T_s^{max} . One can see in

	$\Omega_b h^2$	$\Omega_{\text{dm}} h^2$	H_0	N_{ib}	N_{ii}
M	5.8×10^{-5}	3.0×10^{-4}	0.15	0.04	0.13
F	8.1×10^{-5}	4.1×10^{-4}	0.16	0.03	0.10
	$T_s^{\text{max}}(\text{K})$	Δ_z	$\ln(10^{10} A_{\text{S}})$	R_{ib}	R_{ii}
M	370	4.2×10^{-3}	1.2×10^{-3}	3.4×10^{-3}	3.3×10^{-3}
F	-	9.4×10^{-4}	1.6×10^{-3}	3.6×10^{-3}	3.0×10^{-3}
	n_{S}	τ	γ_{ii}	α_{ib}	α_{ii}
M	9.8×10^{-4}	2.0×10^{-4}	2.5×10^{-3}	7.5×10^{-3}	4.3×10^{-3}
F	1.7×10^{-3}	3.2×10^{-4}	2.5×10^{-3}	1.1×10^{-2}	4.3×10^{-3}

TABLE V: Standard deviations in presence of the ionizing power spectra. The mock data are, as before, four redshifts’ FFTT and Planck-like CMB. Although there is no loss of accuracy compared to Table. IV for the cosmological parameters, the expected constraints on the background reionization parameter Δ_z and T_s^{max} are severely damaged due to the appearance of new degeneracies (see Fig. 18).

Fig. 18 that the two-dimensional posteriors in the planes $(\Delta_z, N_{\text{ib}})$ and $(T_s^{\text{max}}, N_{\text{ib}})$ are indeed degenerated and even multivalued. The “strips” of maximum posterior values are due to the presence of the acoustic oscillations which favour only some peculiar combination of ionizing amplitude and neutral fraction.

When marginalizing over the cosmological and background reionization parameters, Fig. 17 and Table V show that the nuisance parameters N_{ib} , α_{ib} and R_{ib} can actually be inferred. This is not surprising as they encode the dominant contribution for the ionizing power spectra. On the other hand, although the posteriors of N_{ii} , R_{ii} , α_{ii} and γ_{ii} peak at some preferred values, these are significantly biased compared to the fiducial ones. Again, this can be understood from Fig. 4. The P_{ii} contribution only shows up at small scales, typically $\ell \gtrsim 10000$, where the noise power spectrum becomes of comparable amplitude to the signal (see Fig. 5).

Unsurprisingly, the above-mentioned degeneracies are problematic for a Fisher matrix analysis. As before, the only solution to render the Fisher matrix regular was to remove the parameter T_s^{max} ; whereas removing Δ_z would not fix the ill conditioning. As can be seen in Table V, the Fisher method (convolution included) has difficulty to reproduce all of the MCMC results accurately. For some parameters, precisely the ones which remains weakly sensitive to the ionization parameters, the Fisher forecasts match well with the MCMC. This is the case for the standard cosmological parameters (up to $\Omega_b h^2$). For the background reionization parameters, as for instance Δ_z , the Fisher expected variances can be out by a factor five, which slightly bias the expected variance of τ and $\Omega_b h^2$. Turning off T_s^{max} also kills the multimodal behaviour of the likelihood and the Fisher results end up luckily giving the correct results for the ionizing power spectra amplitudes, N_{ii} and N_{ib} .

To summarize, we have found that even in presence of ionizing power spectra, combining multiredshift FFTT data with CMB data can still be used to reconstruct

the background reionization history together with the more usual set of cosmological parameters. The expected variances of the reionization parameters are nevertheless severely damaged compared to no ionizing sources.

IV. CONCLUSION

In this paper, we have quantitatively shown that omniscopes could be used to constrain the background reionization history while being not sensitive to the zero mode of the brightness temperature.

For this purpose, we have considered a simple but consistent reionization model completely determined by the total optical depth τ , the reionization duration Δ_z and the asymptotic spin temperature T_s^{\max} . We have used both Fisher matrix approaches on the three-dimensional power spectrum and MCMC methods on full sky simulated data to forecast the expected variance of all model parameters. Our results suggest that it is crucial to combine multiple redshifts at the EoR with CMB data to keep all degeneracies under control, in particular owing to an accurate determination of $\Omega_b h^2$. When this is not the case, we have shown that the Fisher predictions can be quite inaccurate, eventually being overoptimistic, but also overpessimistic when the conditions for the Cramér-Rao inequalities are no longer met. For those situations, only the MCMC methods ends up being usable.

Within combined data, the perspectives are quite good as the background history can be fully reconstructed, even in the presence of correlated nuisance ionizing sources. Although we have discussed only one kind of FFTT telescope, our results could be easily generalized to other configurations by a proper rescaling of the resolution and noise parameters of Sec. II. Still, our work would need to be extended with a more complete reionization model, eventually adjusted to numerical simulations in order to include a realistic dependence between the reionization parameters and the redshift evolution of the ionization power spectra. Another extension would be the inclusion of exotic reionization sources, such as a

decaying or annihilating dark matter component.

V. ACKNOWLEDGEMENTS

It is a pleasure to thank Alex Hall for fruitful discussions and comments. S.C. is supported by the Wiener Anspach foundation; L.L.H. acknowledges partial support from the European Union FP7 ITN INVISIBLES (Marie Curie Actions, Grant No. PITN-GA-2011-289442), the Galileo Galilei Institute for Theoretical Physics and the INFN for hospitality, the Belgian Federal Science Policy Office through the Interuniversity Attraction Pole Grant No. P7/37 and the FWO-Vlaanderen for a postdoctoral fellowship (Grant No. 1271513N) and for the Grant No. G.0114.10N. C.R. is partially supported by the ESA Belgian Federal PRODEX Grant No. 4000103071 and the Wallonia-Brussels Federation grant ARC No. 11/15-040. The work of M.H.G.T. is partially supported by the grant ARC ‘‘Beyond Einstein: fundamental aspects of gravitational interactions’’.

Appendix A: Boltzmann equations

In this appendix, we recap some of the equations driving the dynamics of the 21-cm brightness fluctuations as they are derived in Ref. [42]. Denoting by $f(\eta, \epsilon)$ the photon distribution function of 21-cm photons, where ϵ is the redshifted energy of 21-cm photons ($T_b = \epsilon f/2$ in the Rayleigh-Jeans approximation), the multipole components of the photon distribution function $F_\ell(\eta, \epsilon, k)$ are defined by

$$\delta f(\eta, \epsilon, \hat{\mathbf{n}}) = 4\pi \sum_{\ell, m} \int \frac{d\mathbf{k}^3}{(2\pi)^{3/2}} (-i)^\ell F_\ell Y_\ell^{m*}(\mathbf{k}) Y_\ell^m(\hat{\mathbf{n}}), \quad (\text{A1})$$

where the Y_ℓ^m are the spherical harmonics. From the perturbed Boltzmann equation, they are found to verify [42]

$$\begin{aligned} F_\ell(\eta_0, \epsilon, k) = & e^{-\tau_c} \left\{ f_\epsilon \left[\Delta_s + \Psi + \frac{r_\epsilon \partial_\eta \Phi}{\mathcal{H}} + (r_\epsilon - 1) (\Delta_{\text{HI}} - \Delta_{T_s} + \Psi) \right] - g_\epsilon \Psi \right\} j_\ell(k\Delta\eta_\epsilon) \\ & - e^{-\tau_c} \left[\frac{r_\epsilon f_\epsilon}{\mathcal{H}} (\partial_\eta v + \mathcal{H}v - k\Psi) + g_\epsilon v + f_\epsilon \frac{T_{\text{rad}}}{T_s - T_{\text{rad}}} (v_\gamma - v) \right]_{\eta_\epsilon} j'_\ell(k\Delta\eta_\epsilon) + (r_\epsilon e^{-\tau_c} f_\epsilon \Delta v)_{\eta_\epsilon} j''_\ell(k\Delta\eta_\epsilon) \\ & - \int_{\eta_\epsilon}^{\eta_0} d\eta (\partial_\eta \tau_c) e^{-\tau_c} \left\{ (F_0 - g_\epsilon \Psi) j_\ell(k\Delta\eta) - g_\epsilon v j'_\ell(k\Delta\eta) + \frac{F_2}{4} [3j''_\ell(k\Delta\eta) + j_\ell(k\Delta\eta)] \right\} \\ & - g_\epsilon \int_{\eta_\epsilon}^{\eta_0} d\eta e^{-\tau_c} \partial_\eta (\Phi + \Psi) j_\ell(k\Delta\eta) - e^{-\tau_c} f_\epsilon \frac{T_{\text{rad}}}{T_s - T_{\text{rad}}} \sum_{\ell'=2}^{\infty} (2\ell' + 1) \Theta_{\ell'} i^{\ell'} P_{\ell'} \left(-\frac{i}{k} \frac{d}{d\eta_\epsilon} \right) j_\ell(k\Delta\eta_\epsilon), \end{aligned} \quad (\text{A2})$$

In this equation, the conformal distance to the redshift of observation is given by $\Delta\eta_\epsilon \equiv \eta_\epsilon - \eta_0$, τ_c is the Thomson

scattering optical depth, τ_ϵ the optical depth of 21 cm

photons and $r_\epsilon \equiv \tau_\epsilon e^{-\tau_\epsilon}/(1 - e^{-\tau_\epsilon})$ encodes the amount of rescattered 21-cm photons. The Legendre polynomials have been denoted P_ℓ while Θ_ℓ stand for the multipole moments of the CMB temperature anisotropies [42]. Both f_ϵ and g_ϵ are functions of ϵ only conveniently defined from the background distribution function

$$f(\eta, \epsilon) \equiv f_\epsilon \frac{1 - e^{-\tau_{21}(\eta)}}{1 - e^{-\tau_\epsilon}}, \quad (\text{A3})$$

and its derivative

$$\epsilon \partial_\epsilon f(\eta, \epsilon) \equiv g_\epsilon \frac{1 - e^{-\tau_{21}(\eta)}}{1 - e^{-\tau_\epsilon}} - \frac{f_\epsilon}{\mathcal{H}(\eta_\epsilon)} \frac{(\partial_\eta \tau_{21}) e^{-\tau_{21}(\eta)}}{1 - e^{-\tau_\epsilon}}. \quad (\text{A4})$$

In the above equations, $\tau_{21}(\eta) \equiv \tau_\epsilon \mathcal{H}(\eta - \eta_\epsilon)$, $\mathcal{H}(x)$ being the Heaviside step function. As discussed in Sec. II A 4, in the small angle limit and assuming $\tau_\epsilon \ll 1$ one recovers Eq. (6). The multipole moments read

$$F_\ell \simeq e^{-\tau_c} \tilde{T}_b [(x_H \Delta_b - x_i \Delta_{x_i}) j_\ell(k \Delta \eta_\epsilon) + x_H \Delta_v j_\ell''(k \Delta \eta_\epsilon)]. \quad (\text{A5})$$

Plugging this equation into Eq. (23) gives Eq. (24).

-
- [1] A. Loeb and R. Barkana, *Ann. Rev. Astron. Astrophys.* **39**, 19 (2001), astro-ph/0010467.
- [2] S. Furlanetto, S. P. Oh, and F. Briggs, *Phys. Rept.* **433**, 181 (2006), astro-ph/0608032.
- [3] R. Barkana and A. Loeb, *Rept. Prog. Phys.* **70**, 627 (2007), astro-ph/0611541.
- [4] J. R. Pritchard and A. Loeb, *Rept. Prog. Phys.* **75**, 086901 (2012), 1109.6012.
- [5] M. Tegmark and M. Zaldarriaga, *Phys. Rev.* **D79**, 083530 (2009), 0805.4414.
- [6] M. Tegmark and M. Zaldarriaga, *Phys. Rev.* **D82**, 103501 (2010), 0909.0001.
- [7] J. B. Peterson, K. Bandura, and U. L. Pen (2006), astro-ph/0606104.
- [8] M. A. Garrett (2009), 0909.3147.
- [9] J. Lazio (2009), 0910.0632.
- [10] S. Rawlings (2011), 1105.6333.
- [11] U.-L. Pen, T.-C. Chang, C. M. Hirata, J. B. Peterson, J. Roy, Y. Gupta, J. Odegova, and K. Sigurdson, *Mon. Not. Roy. Astron. Soc.* **399**, 181 (2009), 0807.1056.
- [12] D. A. Mitchell et al. (2010), 1008.2551.
- [13] S. M. Ord, D. A. Mitchell, R. B. Wayth, L. J. Greenhill, G. Bernardi, S. Gleadow, R. G. Edgar, M. A. Clark, G. Allen, W. Arcus, et al., *PASP* **122**, 1353 (2010), 1010.1733.
- [14] A. R. Parsons, D. C. Backer, G. S. Foster, M. C. H. Wright, R. F. Bradley, N. E. Gugliucci, C. R. Parashare, E. E. Benoit, J. E. Aguirre, D. C. Jacobs, et al., *Astron. J.* **139**, 1468 (2010), 0904.2334.
- [15] J. M. Bittner and A. Loeb, *JCAP* **1104**, 038 (2011), 1006.5460.
- [16] M. G. Santos, M. B. Silva, J. R. Pritchard, R. Cen, and A. Cooray, *Astron. Astrophys.* **527**, A93 (2011), 1009.0950.
- [17] G. Harker, S. Zaroubi, G. Bernardi, M. A. Brentjens, A. de Bruyn, et al., *Mon. Not. Roy. Astron. Soc.* **405**, 2492 (2010), 1003.0965.
- [18] T.-C. Chang, U.-L. Pen, K. Bandura, and J. B. Peterson, *Nature* **466**, 463 (2010), 1007.3709.
- [19] G. Paciga, T.-C. Chang, Y. Gupta, R. Nityanada, J. Odegova, U.-L. Pen, J. B. Peterson, J. Roy, and K. Sigurdson, *Mon. Not. Roy. Astron. Soc.* **413**, 1174 (2011), 1006.1351.
- [20] A. Morandi and R. Barkana (2011), 1102.2378.
- [21] T. Di Matteo, R. Perna, T. Abel, and M. J. Rees, *Astrophys. J.* **564**, 576 (2002), astro-ph/0109241.
- [22] V. Jelic et al., *Mon. Not. Roy. Astron. Soc.* **389**, 1319 (2008), 0804.1130.
- [23] J. D. Bowman, M. F. Morales, and J. N. Hewitt, *Astrophys. J.* **695**, 183 (2009), 0807.3956.
- [24] N. Petrovic and S. P. Oh, *Mon. Not. Roy. Astron. Soc.* **413**, 2103 (2011), 1010.4109.
- [25] G. J. A. Harker, J. R. Pritchard, J. O. Burns, and J. D. Bowman, *Mon. Not. Roy. Astron. Soc.* **419**, 1070 (2012), 1107.3154.
- [26] M. A. Alvarez, E. Komatsu, O. Dore, and P. R. Shapiro, *Astrophys. J.* **647**, 840 (2006), astro-ph/0512010.
- [27] H. Tashiro, N. Aghanim, M. Langer, M. Douspis, S. Zaroubi, et al., *Mon. Not. Roy. Astron. Soc.* **402**, 2617 (2010), 0908.1632.
- [28] V. Jelić, S. Zaroubi, N. Aghanim, M. Douspis, L. V. E. Koopmans, M. Langer, G. Mellema, H. Tashiro, and R. M. Thomas, *Mon. Not. Roy. Astron. Soc.* **402**, 2279 (2010), 0907.5179.
- [29] S. Wyithe and A. Loeb, *Mon. Not. Roy. Astron. Soc.* (2006), astro-ph/0609734.
- [30] S. Furlanetto and A. Lidz, *Astrophys. J.* (2006), astro-ph/0611274.
- [31] C. J. Hogan and M. J. Rees, *Mon. Not. Roy. Astron. Soc.* **188**, 791 (1979).
- [32] D. Scott and M. J. Rees, *Mon. Not. Roy. Astron. Soc.* **247**, 510 (1990).
- [33] P. Madau, A. Meiksin, and M. J. Rees, *Astrophys. J.* **475**, 429 (1997), astro-ph/9608010.
- [34] S. Seager, D. D. Sasselov, and D. Scott, *Astrophys. J.* **523**, L1 (1999), astro-ph/9909275.
- [35] S. Seager, D. D. Sasselov, and D. Scott, *Astrophys. J. Suppl.* **128**, 407 (2000), astro-ph/9912182.
- [36] S. Furlanetto and M. Furlanetto, *Mon. Not. Roy. Astron. Soc.* **379**, 130 (2007), astro-ph/0702487.
- [37] E. Komatsu et al. (WMAP), *Astrophys. J. Suppl.* **192**, 18 (2011), 1001.4538.
- [38] A. Loeb and M. Zaldarriaga, *Phys. Rev. Lett.* **92**, 211301 (2004), astro-ph/0312134.
- [39] S. Bharadwaj and S. S. Ali, *Mon. Not. Roy. Astron. Soc.* **352**, 142 (2004), astro-ph/0401206.
- [40] S. Naoz and R. Barkana, *Mon. Not. Roy. Astron. Soc.* **362**, 1047 (2005), astro-ph/0503196.

- [41] C. M. Hirata and K. Sigurdson, *Mon.Not.Roy.Astron.Soc.* **375**, 1241 (2007), [astro-ph/0605071](#).
- [42] A. Lewis and A. Challinor, *Phys. Rev.* **D76**, 083005 (2007), [astro-ph/0702600](#).
- [43] A. Lewis, *Phys. Rev.* **D76**, 063001 (2007), 0707.2727.
- [44] Y. Mao, M. Tegmark, M. McQuinn, M. Zaldarriaga, and O. Zahn, *Phys. Rev.* **D78**, 023529 (2008), 0802.1710.
- [45] A. Pillepich, C. Porciani, and S. Matarrese, *Astrophys.J.* **662**, 1 (2007), [astro-ph/0611126](#).
- [46] A. Cooray, *Phys. Rev. Lett.* **97**, 261301 (2006), [astro-ph/0610257](#).
- [47] S. Joudaki, O. Dore, L. Ferramacho, M. Kaplinghat, and M. G. Santos, *Phys. Rev. Lett.* **107**, 131304 (2011), 1105.1773.
- [48] S. Chongchitnan and J. Silk (2012), 1205.6799.
- [49] R. Khatri and B. D. Wandelt, *Phys. Rev. Lett.* **100**, 091302 (2008), 0801.4406.
- [50] R. H. Brandenberger, R. J. Danos, O. F. Hernandez, and G. P. Holder, *JCAP* **1012**, 028 (2010), 1006.2514.
- [51] A. Berndsen, L. Pogosian, and M. Wyman, *Mon.Not.Roy.Astron.Soc.* **407**, 1116 (2010), 1003.2214.
- [52] M. Pagano and R. Brandenberger, *JCAP* **1205**, 014 (2012), 1201.5695.
- [53] Y. A. Shchekinov and E. O. Vasiliev, *Mon.Not.Roy.Astron.Soc.* **379**, 1003 (2007), [astro-ph/0604231](#).
- [54] M. Valdes, A. Ferrara, M. Mapelli, and E. Ripamonti, *Mon.Not.Roy.Astron.Soc.* **377**, 245 (2007), [astro-ph/0701301](#).
- [55] E. Borriello, A. Cuoco, and G. Miele, *Phys. Rev.* **D79**, 023518 (2009), 0809.2990.
- [56] D. T. Cumberbatch, M. Lattanzi, and J. Silk, *Phys. Rev.* **D82**, 103508 (2010), 0808.0881.
- [57] A. Natarajan and D. J. Schwarz, *Phys. Rev.* **D80**, 043529 (2009), 0903.4485.
- [58] P. Brax, S. Clesse, and A.-C. Davis (2012), 1207.1273.
- [59] V. Barger, Y. Gao, Y. Mao, and D. Marfatia, *Phys. Lett.* **B673**, 173 (2009), 0810.3337.
- [60] C. Gordon and J. R. Pritchard, *Phys. Rev.* **D80**, 063535 (2009), 0907.5400.
- [61] K. W. Masui and U.-L. Pen, *Phys. Rev. Lett.* **105**, 161302 (2010), 1006.4181.
- [62] P. Adshead, R. Easther, J. Pritchard, and A. Loeb, *JCAP* **1102**, 021 (2011), 1007.3748.
- [63] S. Jester and H. Falcke, *New Astron. Rev.* **53**, 1 (2009), 0902.0493.
- [64] B. Ciardi and P. Madau, *Astrophys. J.* **596**, 1 (2003), [astro-ph/0303249](#).
- [65] S. K. Sethi, *Mon.Not.Roy.Astron.Soc.* **363**, 818 (2005), [astro-ph/0508172](#).
- [66] R. Barkana and A. Loeb, *Mon. Not. Roy. Astron. Soc. Lett.* **363**, L36 (2005), [astro-ph/0502083](#).
- [67] R. M. Thomas and S. Zaroubi, *Mon.Not.Roy.Astron.Soc.* **410**, 1377 (2011), 1009.5441.
- [68] Y. Mao, P. R. Shapiro, G. Mellema, I. T. Iliev, J. Koda, and K. Ahn, *Mon.Not.Roy.Astron.Soc.* **422**, 926 (2012), 1104.2094.
- [69] A. Liu and M. Tegmark, *Phys. Rev.* **D83**, 103006 (2011), 1103.0281.
- [70] A. Liu and M. Tegmark, *Mon.Not.Roy.Astron.Soc.* **419**, 3491 (2012), 1106.0007.
- [71] M. Tegmark, A. Taylor, and A. Heavens, *Astrophys.J.* **480**, 22 (1997), [astro-ph/9603021](#).
- [72] J. R. Pritchard and A. Loeb, *Phys. Rev.* **D82**, 023006 (2010), 1005.4057.
- [73] A. Lewis, A. Challinor, and A. Lasenby, *Astrophys. J.* **538**, 473 (2000), [astro-ph/9911177](#), URL <http://camb.info>.
- [74] A. Lewis and S. Bridle, *Phys. Rev.* **D66**, 103511 (2002), [astro-ph/0205436](#), URL <http://cosmologist.info/cosmomc>.
- [75] A. Challinor and A. Lewis, *Phys.Rev.* **D84**, 043516 (2011), 1105.5292.
- [76] J. R. Pritchard and A. Loeb, *Phys.Rev.* **D78**, 103511 (2008), 0802.2102.
- [77] R. Barkana and A. Loeb, *Astrophys.J.* **624**, L65 (2005), [astro-ph/0409572](#).
- [78] R. Barkana and A. Loeb, *Astrophys.J.* **626**, 1 (2005), [astro-ph/0410129](#).
- [79] M. McQuinn, L. Hernquist, M. Zaldarriaga, and S. Dutta, *Mon.Not.Roy.Astron.Soc.* **381**, 75 (2007), * Brief entry *, 0704.2239.
- [80] O. Zahn, A. Mesinger, M. McQuinn, H. Trac, R. Cen, et al. (2010), 1003.3455.
- [81] A. R. Thompson, J. M. Moran, and G. W. Swenson, Jr., *Interferometry and Synthesis in Radio Astronomy, 2nd Edition* (Wiley-VCH, Weinheim, 2001).
- [82] T. L. Wilson, K. Rohlfs, and S. Hüttemeister, *Tools of Radio Astronomy* (Springer-Verlag, 2009).
- [83] M. Zaldarriaga, S. R. Furlanetto, and L. Hernquist, *Astrophys.J.* **608**, 622 (2004), [astro-ph/0311514](#).
- [84] L. Knox, *Phys.Rev.* **D52**, 4307 (1995), 28 pages, [astro-ph/9504054](#).
- [85] R. Durrer, *The Cosmic Microwave Background* (Cambridge University Press, 2008).
- [86] A. Datta, J. Bowman, and C. Carilli, *Astrophys.J.* **724**, 526 (2010), 1005.4071.
- [87] M. F. Morales, B. Hazelton, I. Sullivan, and A. Beardsley, *Astrophys.J.* **752**, 137 (2012), 1202.3830.
- [88] A. C. Hall and A. Challinor (2012), 1205.6172.
- [89] S. Hamimeche and A. Lewis, *Phys.Rev.* **D77**, 103013 (2008), 0801.0554.
- [90] J. Bond, A. H. Jaffe, and L. Knox, *Astrophys.J.* **533**, 19 (2000), [astro-ph/9808264](#).
- [91] W. J. Percival and M. L. Brown, *Mon.Not.Roy.Astron.Soc.* **372**, 1104 (2006), [astro-ph/0604547](#).
- [92] J.-M. Lamarre, J.-L. Puget, P. A. R. Ade, F. Bouchet, G. Guyot, A. E. Lange, F. Pajot, A. Arondel, K. Benabed, J.-L. Beney, et al., *Astron. & Astrophys.* **520**, A9 (2010).
- [93] P. A. R. Ade, G. Savini, R. Sudiwala, C. Tucker, A. Catalano, S. Church, R. Colgan, F. X. Desert, E. Gleeson, W. C. Jones, et al., *Astron. & Astrophys.* **520**, A11 (2010).